ATLAS NOTE

ATLAS-CONF-2012-092

July 6, 2012

Observation of an excess of events in the search for the Standard Model Higgs boson in the $H \to ZZ^{(*)} \to 4\ell$ channel with the ATLAS detector

The ATLAS Collaboration

Abstract

This note presents a search for the Standard Model Higgs boson in the decay channel $H \to ZZ^{(*)} \to \ell^+\ell^-\ell'^+\ell'^-$, where $\ell, \ell' = e$ or μ, using 4.8 fb^{-1} and 5.8 fb^{-1} of proton-proton collisions at $\sqrt{s} = 7$ TeV and 8 TeV, respectively, recorded with the ATLAS detector. The four-lepton invariant mass distribution is compared with Standard Model background expectations to derive upper limits on the cross section of a Standard Model Higgs boson with a mass between 110 GeV and 600 GeV. The mass ranges 131 – 162 GeV and 170 – 460 GeV are excluded at the 95% confidence level, while the expected exclusion ranges at the 95% confidence level are 124 – 164 GeV and 176 – 500 GeV. An excess of events is observed around $m_H = 125$ GeV, whose local p_0 value is 0.029% (3.4 standard deviations) in the combined analysis of the two datasets.

1 Introduction

The Higgs mechanism in the context of the Standard Model (SM) is the source of electroweak symmetry breaking and results in the appearance of the Higgs boson [1–3], which remains the only unobserved particle of the Standard Model. Direct searches performed at the CERN Large Electron-Positron Collider (LEP) excluded at 95% confidence level (CL) the production of a SM Higgs boson with mass, m_H, less than 114.4 GeV [4]. The searches at the Fermilab Tevatron $p\bar{p}$ collider have excluded at 95% CL the region 147 GeV $< m_H <$ 179 GeV [5]. At the LHC, the ATLAS experiment using 4.9 fb^{-1} of data at $\sqrt{s} = 7$ TeV collected in 2011 [6] has excluded [7] the m_H regions 112.9 − 115.5 GeV, 131 − 238 GeV and 251 − 466 GeV at the 95% CL. The CMS results [8] based to up to 4.8 fb^{-1} of data have excluded at the 95% CL the m_H range 127 − 600 GeV [9].

The search for the SM Higgs boson through the decay $H \to ZZ^{(*)} \to \ell^+\ell^-\ell'^+\ell'^-$, where $\ell, \ell' = e$ or μ, provides good sensitivity over a wide mass range. The largest background to this search comes from continuum $(Z^{(*)}/\gamma^*)(Z^{(*)}/\gamma^*)$ production, referred to as $ZZ^{(*)}$ hereafter. For low masses, there are also important background contributions from Z + jets and $t\bar{t}$ production, where the additional charged lepton candidates arise either from decays of hadrons with b- or c-quark content or from mis-identification of jets. Previous results from ATLAS in this channel [6] excluded the mass regions 134 − 156 GeV, 182 − 233 GeV, 256 − 265 GeV and 268 − 415 GeV at 95% CL with 4.8 fb^{-1} of $\sqrt{s} = 7$ TeV data. The corresponding search from CMS [8] excluded at 95% CL the mass regions 134–158 GeV, 180–305 GeV and 340 − 465 GeV.

This note updates the results presented in Ref. [6], with a new analysis of the $\sqrt{s} = 7$ TeV data corresponding to an integrated luminosity of 4.8 fb^{-1} collected in 2011, combined with the first analysis of $\sqrt{s} = 8$ TeV data corresponding to an integrated luminosity of 5.8 fb^{-1} collected between April and June 2012 [10, 11]. The analysis selection has been optimised with respect to the one described in Ref. [6] to enhance the sensitivity to a low mass Higgs boson. The $\sqrt{s} = 8$ TeV data analysis benefits from substantial improvements in the electron reconstruction and identification compared to the one used for the $\sqrt{s} = 7$ TeV data, which have not yet been reprocessed to take advantage of these improvements.

In the following, the ATLAS detector is briefly described in Section 2, and the signal and background simulation is presented in Section 3. The analysis of the $\sqrt{s} = 8$ TeV data collected between March and June 2012 is discussed in Section 4 and that of the $\sqrt{s} = 7$ TeV data collected in 2011 is described in Section 5. After a description of the systematic uncertainties in Section 6, Section 7 presents the result of the combined analysis of the two datasets.

2 The ATLAS Detector

The ATLAS detector [12] is a multi-purpose particle physics detector with approximately forward-backward symmetric cylindrical geometry[1]. The inner tracking detector (ID) [13] covers $|\eta| < 2.5$ and consists of a silicon pixel detector, a silicon micro-strip detector, and a transition radiation tracker. The ID is surrounded by a thin superconducting solenoid providing a 2 T axial magnetic field. A high-granularity lead/liquid-argon (LAr) sampling calorimeter [14] measures the energy and the position of electromagnetic showers with $|\eta| < 3.2$. LAr sampling calorimeters are also used to measure hadronic showers in the end-cap ($1.5 < |\eta| < 3.2$) and forward ($3.1 < |\eta| < 4.9$) regions, while an iron/scintillator tile calorimeter [15] measures hadronic showers in the central region ($|\eta| < 1.7$). The muon spectrometer (MS) [16] surrounds the calorimeters and consists of three large superconducting air-core toroid magnets,

[1] ATLAS uses a right-handed coordinate system with its origin at the nominal interaction point. The z-axis is along the beam pipe, the x-axis points to the centre of the LHC ring and the y-axis is defined as pointing upwards. Polar coordinates (r,ϕ) are used in the transverse plane, ϕ being the azimuthal angle around the beam pipe. The pseudo-rapidity η is defined as $\eta = -\ln[\tan(\theta/2)]$ where θ is the polar angle.

each with eight coils, a system of precision tracking chambers ($|\eta| < 2.7$), and fast tracking chambers for triggering. A three-level trigger system [17] selects events to be recorded for offline analysis.

3 Signal and Background Simulation

The $H \to ZZ^{(*)} \to 4\ell$ signal is modelled using the Powheg Monte Carlo (MC) event generator [18, 19], which calculates separately the gluon fusion and vector-boson fusion production mechanisms with matrix elements up to next-to-leading order (NLO). The Higgs boson transverse momentum (p_{T}) spectrum in the gluon fusion process follows the calculation of Ref. [20], which includes QCD corrections up to NLO and QCD soft-gluon re-summations up to next-to-next-to-leading logarithm (NNLL). Powheg is interfaced to Pythia [21, 22] for showering and hadronization, which in turn is interfaced to Photos [23, 24] for quantum electrodynamics (QED) radiative corrections in the final state. Pythia is used to simulate the production of a Higgs boson in association with a W or a Z boson.

The Higgs boson production cross sections and decay branching ratios, as well as their uncertainties, are taken from Refs. [25, 26]. The cross sections for the gluon-fusion process have been calculated to next-to-leading order (NLO) [27–29], and next-to-next-to-leading order (NNLO) [30–32] in QCD. In addition, QCD soft-gluon re-summations calculated in the next-to-next-to-leading log (NNLL) approximation are applied for the gluon-fusion process [33]. NLO electroweak (EW) radiative corrections are also applied [34, 35]. These results are compiled in Refs. [36–38] assuming factorisation between QCD and EW corrections. The cross sections for vector-boson fusion processes are calculated with full NLO QCD and EW corrections [39–41], and approximate NNLO QCD corrections are available [42]. The cross sections for the associated WH/ZH production processes are calculated at NLO [43] and at NNLO [44] in QCD, and NLO EW radiative corrections [45] are applied.

The Higgs boson decay branching ratios [46] to the different four-lepton final states is provided by Prophecy4f [47, 48], which includes the complete NLO QCD+EW corrections, interference effects between identical final-state fermions, and leading two-loop heavy Higgs boson corrections to the four-fermion width. Table 1 gives the production cross sections and branching ratios for $H \to ZZ^{(*)} \to 4\ell$, which are used to normalise the signal MC, for several Higgs boson masses.

The QCD scale uncertainties for $m_{\mathrm{H}} = 125$ GeV [25] amount to $^{+7}_{-8}\%$ for the gluon-fusion process and $\pm 1\%$ for the vector-boson fusion and associated WH/ZH production processes. The uncertainty of the production cross section due to uncertainties of the parton distribution function (PDF) and α_s is $\pm 8\%$ for gluon-initiated processes and $\pm 4\%$ for quark-initiated processes, estimated by following the prescription in Ref. [49] and by using the PDF sets of CTEQ [50], MSTW [51] and NNPDF [52]. The PDF uncertainties are assumed to be 100% correlated among processes with identical initial states, regardless of these being signal or background [49–53].

The cross section calculations do not take into account the width of the Higgs boson, which is implemented through a relativistic Breit-Wigner line shape applied at the event-generator level. In the absence of a full calculation, the possible size of such effects is included as an extra signal normalisation systematic uncertainty for $m_H \geq 300$ GeV, on top of the one presented in Table 1, following a parametrisation as a function of m_H: $150\% \times m_H^3$[TeV] [26].

The $ZZ^{(*)}$ continuum background is modelled using Powheg [54] for quark-antiquark annihilation and `gg2ZZ` [55] for gluon fusion, normalised to the mcfm prediction [56]. The QCD scale uncertainty has a $\pm 5\%$ effect on the expected $ZZ^{(*)}$ background, and the effect due to the PDF and α_s uncertainties is $\pm 4\%$ ($\pm 8\%$) for quark-initiated (gluon-initiated) processes. In addition, the shape uncertainty of the four-lepton invariant mass spectrum has been assigned as discussed in Ref. [26]. For the simulation of τ lepton decays Tauola [57, 58] is used. The Z + jets production is modelled using Alpgen [59] and is divided into two sources: Z + light jets, which includes $Zc\bar{c}$ in the massless c-quark approximation and $Zb\bar{b}$ from parton showers, and $Zb\bar{b}$ using matrix element calculations that take into account the b-quark

Table 1: Higgs boson production cross sections for gluon fusion, vector-boson fusion and associated production with a W or Z boson in pp collisions at $\sqrt{s}$ of 7 TeV and 8 TeV [25]. The quoted uncertainties correspond to the total theoretical systematic uncertainties. The production cross section for the associated production with a W or Z boson is negligibly small for $m_H > 300$ GeV. The decay branching ratio for $H \to 4\ell$, with $\ell = e$ or μ, is reported in the last column [25].

m_H [GeV]	$\sigma(gg \to H)$ [pb]	$\sigma(qq' \to Hqq')$ [pb]	$\sigma(q\bar{q} \to WH)$ [pb]	$\sigma(q\bar{q} \to ZH)$ [pb]	$\mathrm{BR}\left(H \to ZZ^{(*)} \to 4\ell\right)$ [10^{-3}]
			$\sqrt{s} = 7$ TeV		
125	$15.3^{+3.0}_{-2.3}$	1.21 ± 0.03	$0.57^{+0.02}_{-0.03}$	0.32 ± 0.02	0.13
130	$14.1^{+2.7}_{-2.1}$	1.15 ± 0.03	0.50 ± 0.02	0.28 ± 0.01	0.19
190	$5.9^{+1.0}_{-0.9}$	0.69 ± 0.02	0.125 ± 0.005	0.074 ± 0.004	0.94
400	$2.03^{+0.32}_{-0.33}$	$0.162^{+0.009}_{-0.005}$	–	–	1.21
600	0.37 ± 0.06	$0.058^{+0.005}_{-0.002}$	–	–	1.23
			$\sqrt{s} = 8$ TeV		
125	19.5 ± 2.9	$1.56^{+0.04}_{-0.05}$	0.70 ± 0.03	0.39 ± 0.02	0.13
130	18.1 ± 2.6	1.49 ± 0.04	0.61 ± 0.03	0.35 ± 0.02	0.19
190	7.9 ± 1.1	$0.91^{+0.03}_{-0.02}$	0.156 ± 0.007	0.094 ± 0.006	0.94
400	2.9 ± 0.4	0.25 ± 0.01	–	–	1.21
600	0.5 ± 0.1	0.097 ± 0.004	–	–	1.23

mass. The MLM [60] matching scheme is used to remove any double counting of identical jets produced via the matrix element calculation and the parton shower, but this scheme is not implemented for b-jets. Therefore, $b\bar{b}$ pairs with separation $\Delta R = \sqrt{(\Delta\phi)^2 + (\Delta\eta)^2} > 0.4$ between the b-quarks are taken from the matrix-element calculation, whereas for $\Delta R < 0.4$ the parton-shower $b\bar{b}$ pairs are used. In this search the Z + jets background is normalised using control samples from data. For comparison between data and simulation, the QCD NNLO FEWZ [61,62] and MCFM cross section calculations are used for inclusive Z boson and $Zb\bar{b}$ production, respectively. The $t\bar{t}$ background is modelled using MC@NLO [63] and is normalised to the approximate NNLO cross section calculated using HATHOR [64]. The effect of the QCD scale uncertainty of the cross section is $^{+4}_{-9}\%$, while the effect of PDF and α_s uncertainties is $\pm 7\%$. Both ALPGEN and MC@NLO are interfaced to HERWIG [65] for parton shower hadronization and to JIMMY [66] for the underlying event simulation.

Generated events are fully simulated using the ATLAS detector simulation [67] within the GEANT4 framework [68]. Additional pp interactions in the same and nearby bunch crossings (pile-up) are included in the simulation. The MC samples are re-weighted to reproduce the observed distribution of the mean number of interactions per bunch crossing in the data.

4 Analysis of $\sqrt{s} = 8$ TeV data

The data are subjected to quality requirements: events recorded during periods when the relevant detector components were not operating normally are rejected. The resulting integrated luminosity is 5.8 fb^{-1}.

4.1 Lepton Reconstruction/Identification and Event Selection

The data considered in this analysis are selected using single-lepton or di-lepton triggers. For the single-muon trigger the transverse momentum p_{T} threshold is 24 GeV, while for the single-electron trigger the transverse energy, E_{T}, threshold is 24 GeV. For the di-muon triggers the thresholds are $p_{\mathrm{T}} = 13$ GeV

for each muon or $p_{\mathrm{T1}} = 18$ GeV, $p_{\mathrm{T2}} = 8$ GeV in the case of the asymmetric di-muon trigger, while for the di-electron triggers the thresholds are $E_{\mathrm{T}} = 12$ GeV for each electron.

Electron candidates consist of clusters of energy deposited in the electromagnetic calorimeter that are associated to ID tracks. For the 2012 LHC data taking, the electron reconstruction algorithm has been improved with respect to 2011, improving the performance at low p_{T}. The ATLAS track pattern recognition and fit procedure were updated to account for energy losses due to bremsstrahlung, and the track-to-cluster matching algorithm was improved to be less sensitive to bremsstrahlung losses. Furthermore, all tracks associated to electromagnetic clusters are re-fitted using a Gaussian-Sum Filter [69], which allows for bremsstrahlung energy losses.

Electron candidates must have a well-reconstructed ID track pointing to the corresponding cluster, and the cluster should satisfy a set of identification criteria [70] that requires the longitudinal and transverse shower profiles to be consistent with those expected for electromagnetic showers. These identification criteria were optimised to maintain good performance in high pile-up conditions, and to take advantage of the new electron reconstruction. The electron transverse momentum is computed from the cluster energy and the track direction at the interaction point.

Muon candidates are formed by matching reconstructed ID tracks with either complete or partial tracks reconstructed in the MS [71]. If a complete track is present, the two independent momentum measurements are combined; otherwise the momentum is measured using the ID or the MS information alone. The muon reconstruction/identification coverage is extended by using tracks reconstructed in the forward region ($2.5 < |\eta| < 2.7$) of the MS, which is outside the ID coverage. In the centre of the barrel region ($|\eta| < 0.1$), which lacks MS geometrical coverage, ID tracks with $p_{\mathrm{T}} > 15$ GeV are identified as muons using the profile of the associated energy deposits in the calorimeter.

This analysis searches for Higgs boson candidates by selecting two same-flavour, opposite-sign lepton pairs in an event. The impact parameter of the leptons along the beam axis is required to be within 10 mm of the reconstructed primary vertex. To reject cosmic rays, muon tracks are required to have a transverse impact parameter, defined as the impact parameter in the bending plane with respect to the primary vertex, of less than 1 mm. The primary vertex is defined as the reconstructed vertex with the highest $\sum p_{\mathrm{T}}^2$ of associated tracks among the reconstructed vertices with at least three associated tracks.

Each electron (muon) must satisfy $p_{\mathrm{T}} > 7$ GeV ($p_{\mathrm{T}} > 6$ GeV) and be measured in the pseudo-rapidity range $|\eta| < 2.47$ ($|\eta| < 2.7$). The most energetic lepton in the quadruplet must satisfy $p_{\mathrm{T}} > 20$ GeV, and the second (third) lepton in p_{T} order must satisfy $p_{\mathrm{T}} > 15$ GeV ($p_{\mathrm{T}} > 10$ GeV). The leptons are required to be separated from each other by $\Delta R > 0.1$ if they are of the same flavour and $\Delta R > 0.2$ otherwise. The same-flavour and opposite-sign lepton pair closest to the Z boson mass (m_Z) is the leading di-lepton, its invariant mass, denoted by m_{12}, is required to be between 50 and 106 GeV. The remaining same-flavour, opposite-sign lepton pair is the sub-leading di-lepton and its invariant mass, m_{34}, is required to be in the range $m_{\mathrm{min}} < m_{34} < 115$ GeV, where the value of m_{min} depends on the reconstructed four-lepton invariant mass, $m_{4\ell}$, and is shown in Table 2. All possible same-flavour opposite-charge di-lepton combinations in the quadruplet must satisfy $m_{\ell\ell} > 5$ GeV. Four different analysis sub-channels ($4e$, $2e2\mu$, $2\mu2e$, 4μ) ordered by the flavour of the leading di-lepton are defined. Data quality requirements result in slightly different integrated luminosities, 5.8 fb^{-1}, 5.8 fb^{-1} and 5.9 fb^{-1} for the 4μ, $2e2\mu/2\mu2e$ and $4e$ sub-channels, respectively.

Table 2: The lower thresholds applied to m_{34} for reference values of $m_{4\ell}$. For $m_{4\ell}$ values between these reference values the selection requirement is obtained via linear interpolation.

$m_{4\ell}$ [GeV]	≤120	130	150	160	165	180	≥190
m_{min} threshold [GeV]	17.5	22.5	30	30	35	40	50

The Z + jets and $t\bar{t}$ background contributions are further reduced by applying impact parameter as well as track- and calorimeter-based isolation requirements on the leptons. The normalised track isolation discriminant is defined as the sum of the transverse momenta of tracks, Σp_{T}, inside a cone of $\Delta R < 0.2$ around the lepton, excluding the lepton track, divided by the lepton p_{T}. The tracks considered in the sum are of good quality; i.e., they have at least four hits in the pixel and silicon strip detectors ("silicon hits") and $p_{\mathrm{T}} > 1$ GeV for muons, and at least nine silicon hits, one hit in the innermost pixel layer (the b-layer) and $p_{\mathrm{T}} > 0.4$ GeV for electrons. Each lepton is required to have a normalised track isolation smaller than 0.15.

The normalised calorimetric isolation for electrons is computed as the sum of the positive-energy topological clusters with a reconstructed barycenter falling in a cone of $\Delta R < 0.2$ around the candidate electron cluster divided by the electron p_{T}. The cut value is 0.20. The cells within 0.125×0.175 in $\eta \times \phi$ around the electron barycenter are excluded. The algorithm for topological clusters suppresses noise by keeping only those cells with a significant energy deposit and their neighbouring cells. The ambient energy deposition in the event from pileup as well as from the underlying event is corrected for by calculating the transverse energy density from low-p_{T} jets, averaged over azimuth in two η regions, and subtracting it from the isolation cone transverse energy. In the case of muons, the normalised calorimetric isolation discriminant is defined as the sum of the calorimeter cells, ΣE_T, inside a cone of $\Delta R < 0.2$ around the muon direction, divided by the muon p_{T}. Muons are required to have a normalised calorimetric isolation less than 0.30 (0.15 in case of muons without an ID track). For both the track- and calorimeter-based isolation any contributions arising from other leptons of the quadruplet are subtracted. The impact parameter significance, defined as the impact parameter divided by its uncertainty, d_0/σ_{d_0}, for all muons (electrons) is required to be lower than 3.5 (6.5). The electron impact parameter is affected by bremsstrahlung and it thus has a broader distribution.

The combined signal reconstruction and selection efficiency for $m_H = 130$ GeV ($m_H = 360$ GeV) is 41% (67%) for the 4μ channel, 27% (59%) for the $2e2\mu/2\mu2e$ channel and 23% (51%) for the $4e$ channel. The final discriminating variable for this search is $m_{4\ell}$. The invariant mass resolution is further improved by applying a Z-mass constraint to the leading di-lepton for $m_{4\ell} < 190$ GeV and to both di-leptons for higher masses. The Z line-shape and the experimental uncertainty in the di-lepton mass are accounted for in the Z-mass constraint. Figure 1 presents the $m_{4\ell}$ distributions before and after the Z mass constraint, for a simulated signal sample with $m_H = 130$ GeV, at $\sqrt{s} = 8$ TeV. The width of the reconstructed Higgs boson mass distribution is dominated by the experimental resolution for $m_H < 350$ GeV, while for higher m_H the reconstructed width is dominated by the natural width of the Higgs boson. The predicted natural width of the Higgs boson is approximately 29 GeV at $m_H = 400$ GeV .

4.2 Background Estimation

The expected background yield and its composition is estimated using MC simulation normalised to the theoretical cross section for $ZZ^{(*)}$ production and by data-driven methods for the $\ell\ell$ + jets and $t\bar{t}$ processes. The background composition depends on the flavour of the sub-leading di-lepton and different approaches are taken for the $\ell\ell + \mu\mu$ and the $\ell\ell + ee$ final states.

4.2.1 $\ell\ell + \mu\mu$ background

The number of $t\bar{t}$ and Z + jets (dominated by $Zb\bar{b}$) background events in the signal region is estimated using a control region with an enhanced $b\bar{b}$ contribution. The control region is obtained by modifying the event selection as follows: no isolation requirement is applied to leptons in the sub-leading pair, and at least one of the sub-leading leptons is required to fail the impact parameter significance requirement. These modifications remove $ZZ^{(*)}$ contributions, and allow both the $t\bar{t}$ and Z + jets backgrounds to be estimated simultaneously.

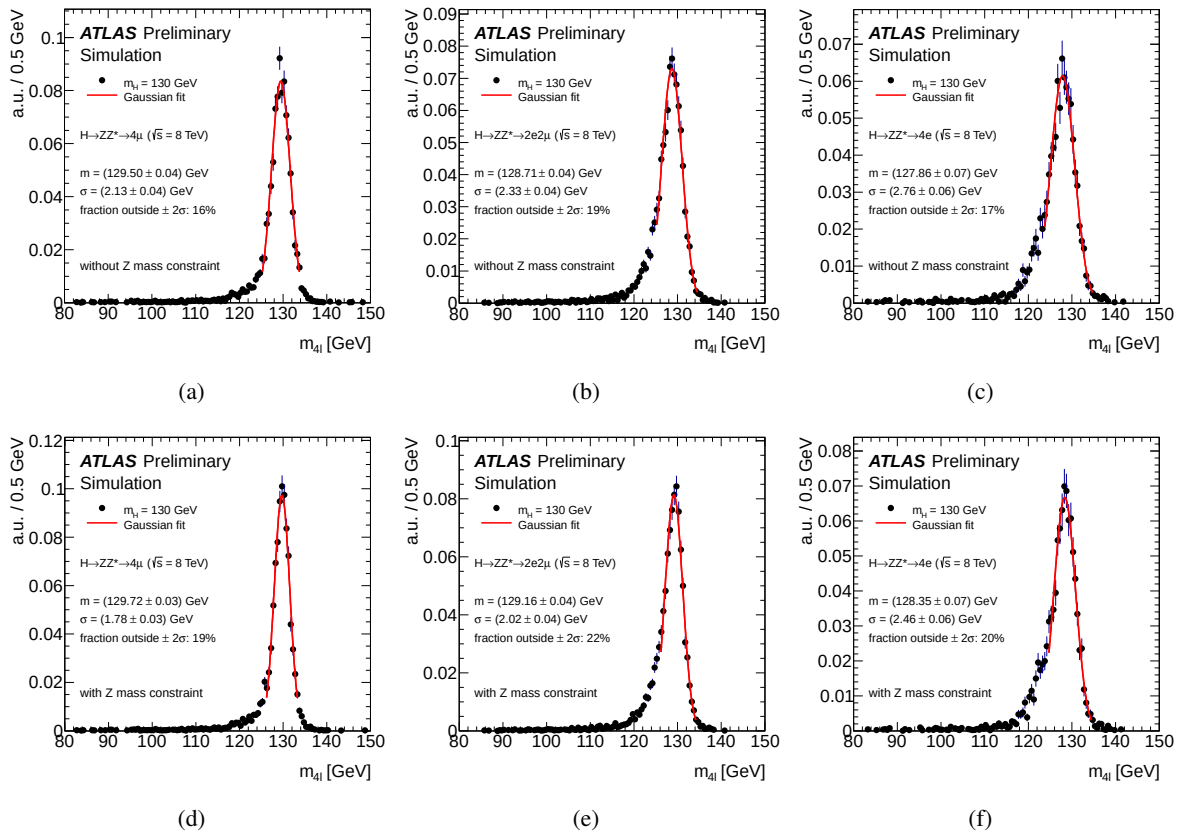

Figure 1: Invariant mass distributions for simulated (a) $H \to ZZ^{(*)} \to 4\mu$, (b) $H \to ZZ^{(*)} \to 2e2\mu$ and (c) $H \to ZZ^{(*)} \to 4e$ events for $m_H = 130$ GeV, at $\sqrt{s} = 8$ TeV. The fitted range for the Gaussian is chosen to be: -2σ to 2σ (-1.5σ to 2.5σ) for the 4μ ($2e2\mu/4e$) channel. The slightly reduced mean values arise from radiative losses which are more explicit in channels involving electrons [70]. In (d), (e) and (f) the corresponding results after applying the Z mass constraint are shown.

As shown in Fig. 2, the m_{12} distribution is fitted using a second order Chebychev polynomial for the $t\bar{t}$ component and a Breit-Wigner line-shape convolved with a Crystal-Ball resolution function for the Z + jets component. The shapes used in the fit are obtained from MC. The number of events in the control region is then extrapolated to the signal region using a transfer factor obtained from MC. The MC description of the selection efficiency has been verified with data using a control region obtained by requiring a Z and exactly one extra muon. This Z is selected using the leading di-lepton requirements of this analysis for the two highest p_{T} same-flavor opposite sign leptons. The systematic errors associated to the extrapolation from the control region to the signal region are comparable with the statistical errors of the fit.

The $t\bar{t}$ background is cross-checked using a control region defined by selecting events with an $e^{\pm}\mu^{\mp}$ di-lepton pair with an invariant mass between 50 and 106 GeV, accompanied by an opposite sign di-muon. Events with a Z candidate decaying to a pair of electrons or muons, in the aforementioned mass range, are excluded. Isolation and impact parameter requirements are applied only to the leptons of the $e\mu$ pair. In data, 16 $e^{\pm}\mu^{\mp} + \mu^{+}\mu^{-}$ events are observed, to be compared with 18.9 ± 1.1 expected from MC.

The expected $\ell\ell + \mu\mu$ background yields in the signal region are summarised in Table 4.

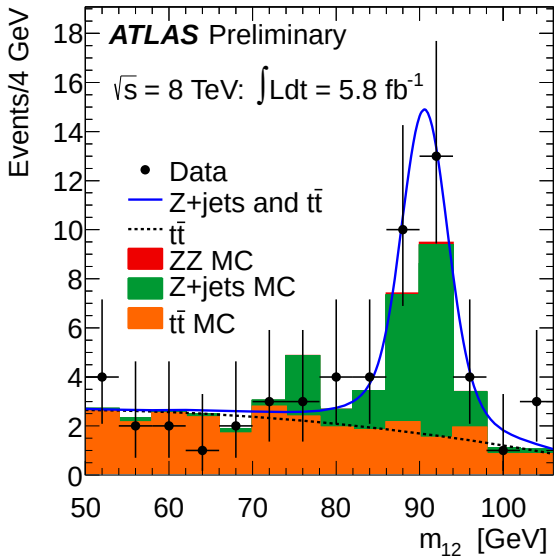

Figure 2: Distribution of m_{12}, for $\sqrt{s} = 8$ TeV, in the control region where the isolation requirements are not applied to the two sub-leading muons, and at least one of these muons fails the impact parameter significance requirement. The fit used to obtain the yields for $t\bar{t}$ and Z + jets is presented, the MC expectations are also shown for comparison.

4.2.2 $\ell\ell + ee$ background

A sample of reconstruction-level objects identified as electron candidates will contain true isolated electrons, electrons from heavy flavour semi-leptonic decays (Q), electrons from photon conversion (γ) or light jets mis-reconstructed as electrons and denoted as fake electrons (f).

An $\ell\ell + ee$ background control region is formed by relaxing the electron selection criteria for the electrons of the sub-leading pair. The different sources of electron background are then separated into reconstruction categories which are electron-like (E), conversion-like (C) and fake-like (F), using appropriate discriminating variables [72]. The variables used are: the number of b-layer hits ($n_{\text{hits}}^{\text{blayer}}$), the fraction of high threshold hits in the Transition Radiation Tracker ($\text{TRT}_{\text{Ratio}}$), the energy in the first layer of the electromagnetic calorimeter (f_1) and the lateral containment of the cluster along ϕ in the second layer of the electromagnetic calorimeter (R_ϕ). The variable $n_{\text{hits}}^{\text{blayer}}$ is used to identify converted photons, and the latter three variables are used to discriminate electrons from hadrons. The numbers of observed events in each category of the control region are presented in Table 3. The expected numbers of events from MC are also given for comparison. Since only events from this control region can enter the signal region, this method directly accounts for most of the fluctuations in data. The efficiency needed to extrapolate the background yield of each category from the control region to the signal region is obtained from MC. This method estimates the sum of Z + jets and $t\bar{t}$ background contributions. As a cross-check the same method is also applied to a similar control region containing same-sign sub-leading di-electrons.

The $\ell\ell + ee$ background is also estimated using a control region with same-sign sub-leading di-electrons, where the three highest p_{T} leptons satisfy all the analysis criteria and the remaining electron is required to only fulfill the good track criteria (silicon hits >= 7 and pixel hits >= 1) and the lateral containment of the cluster energy along η (R_η). This method will be referred to as $3\ell + \ell$ hereafter. In this case a simultaneous fit of templates, obtained from the $n_{\text{hits}}^{\text{blayer}}$ and the $\text{TRT}_{\text{Ratio}}$ distributions, is used to estimate the yields for the different truth components: f, γ and Q. The templates used are obtained from MC. The fits for the $2\mu 2e$ and $4e$ sub-channels are presented in Fig. 3. Additional checks are performed

Table 3: The observed yields of the various categories in the $\ell\ell + ee$ control region for $\sqrt{s} = 8$ TeV. Events are classified according to whether the electron candidates of the sub-leading di-electrons are: electron-like (E), conversion-like (C) and fake-like (F). For comparison the MC expectations are also shown. The di-lepton categorisation in reconstruction categories is ordered in p_{T}.

	$4e$		$2\mu 2e$	
	Data	MC	Data	MC
EE	32	22.7±4.8	31	24.9±5.0
EC	6	6.0±2.5	2	1.9±1.4
EF	18	19.0±4.4	26	15.3±3.9
CE	4	8.8±3.0	6	5.1±2.3
CC	1	5.3±2.3	6	4.2±2.0
CF	12	8.8±3.0	15	15.3±3.9
FE	16	5.7±2.4	12	8.4±2.9
FC	6	6.5±2.6	7	4.3±2.1
FF	12	17.4±4.2	16	33.6±5.8
Total	107	100±10	121	113±11

by replacing the $\mathrm{TRT}_{\mathrm{Ratio}}$ with f_1 or the distance in η between the extrapolated impact point of the track on the calorimeter and the cluster barycenter using the strips ($\Delta\eta_1$). The difference in the results is taken into account as a systematic error.

Finally, the $\ell\ell + ee$ background is also estimated by performing the full analysis but selecting same-sign pairs for the sub-leading di-electrons. In this case, there remain 4 (3) events below $m_{4\ell} = 160$ GeV in the $4e$ ($2\mu 2e$) sub-channel.

The expected $\ell\ell + ee$ background yields in the signal region are summarised in Table 4.

4.2.3 Summary of background estimates

The results of all the background estimation methods are summarised in Table 4. The m_{12} and m_{34} distributions, for events selected by the analysis when relaxing the isolation and impact parameter requirements for the sub-leading di-lepton, are presented in Fig. 4. The events are divided according to the flavour of the sub-leading lepton pair into $\ell\ell + \mu\mu$ and $\ell\ell + ee$ samples. In Figs. 4(a) and 4(c) the m_{12} and m_{34} distributions are presented for $\ell\ell + \mu\mu$ events, while in Figs. 4(b) and 4(d) the corresponding distributions are presented for $\ell\ell + ee$ events. The shape and normalisation of the backgrounds discussed earlier are in good agreement with data. This is observed both for large values of m_{34}, where the $ZZ^{(*)}$ background dominates, and for low m_{34} values.

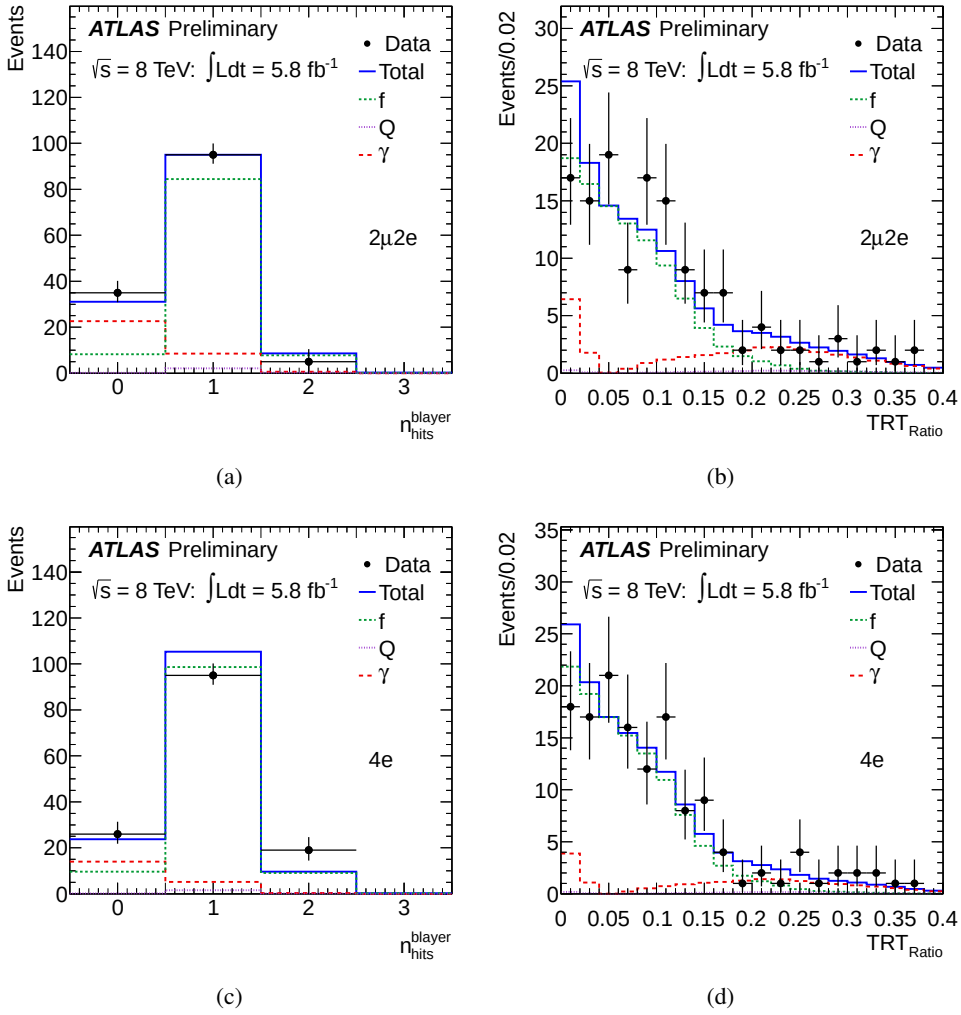

Figure 3: The results of a simultaneous fit to (a) $n_{\text{hits}}^{\text{blayer}}$ and (b) $\text{TRT}_{\text{Ratio}}$ for the background components in the $2\mu 2e$ channel. In (c) and (d) the corresponding results for the $4e$ channel are given. The sources of background electrons are denoted as: light jets faking an electron (f), photon conversions (γ) and electrons from heavy quark semi-leptonic decays (Q).

Table 4: Summary of the background estimates for the $\sqrt{s} = 8$ TeV data. The "†" symbol indicates the estimated number of events used for the background normalisation, the others being cross-checks. The first uncertainty is statistical, while the second is systematic.

Method	Estimated number of events
4μ	
m_{12} fit: Z + jets contribution	$0.51\pm 0.13 \pm 0.16^{\dagger}$
m_{12} fit: $t\bar{t}$ contribution	$0.044\pm 0.015\pm 0.015^{\dagger}$
$t\bar{t}$ from $e^{\pm}\mu^{\mp} + \mu^{\pm}\mu^{\mp}$	$0.058\pm 0.015\pm 0.019$
$2e2\mu$	
m_{12} fit: Z + jets contribution	$0.41\pm 0.10 \pm 0.13^{\dagger}$
m_{12} fit: $t\bar{t}$ contribution	$0.040\pm 0.013\pm 0.013^{\dagger}$
$t\bar{t}$ from $e^{\pm}\mu^{\mp} + \mu^{\pm}\mu^{\mp}$	$0.051\pm 0.013\pm 0.017$
$2\mu 2e$	
$\ell\ell + e^{\pm}e^{\mp}$	$4.9\pm 0.8 \pm 0.7^{\dagger}$
$\ell\ell + e^{\pm}e^{\pm}$	$4.1\pm 0.6 \pm 0.8$
$3\ell + \ell$ (same-sign)	$3.5\pm 0.5 \pm 0.5$
$4e$	
$\ell\ell + e^{\pm}e^{\mp}$	$3.9\pm 0.7 \pm 0.8^{\dagger}$
$\ell\ell + e^{\pm}e^{\pm}$	$3.1\pm 0.5 \pm 0.6$
$3\ell + \ell$ (same-sign)	$3.0\pm 0.4 \pm 0.4$

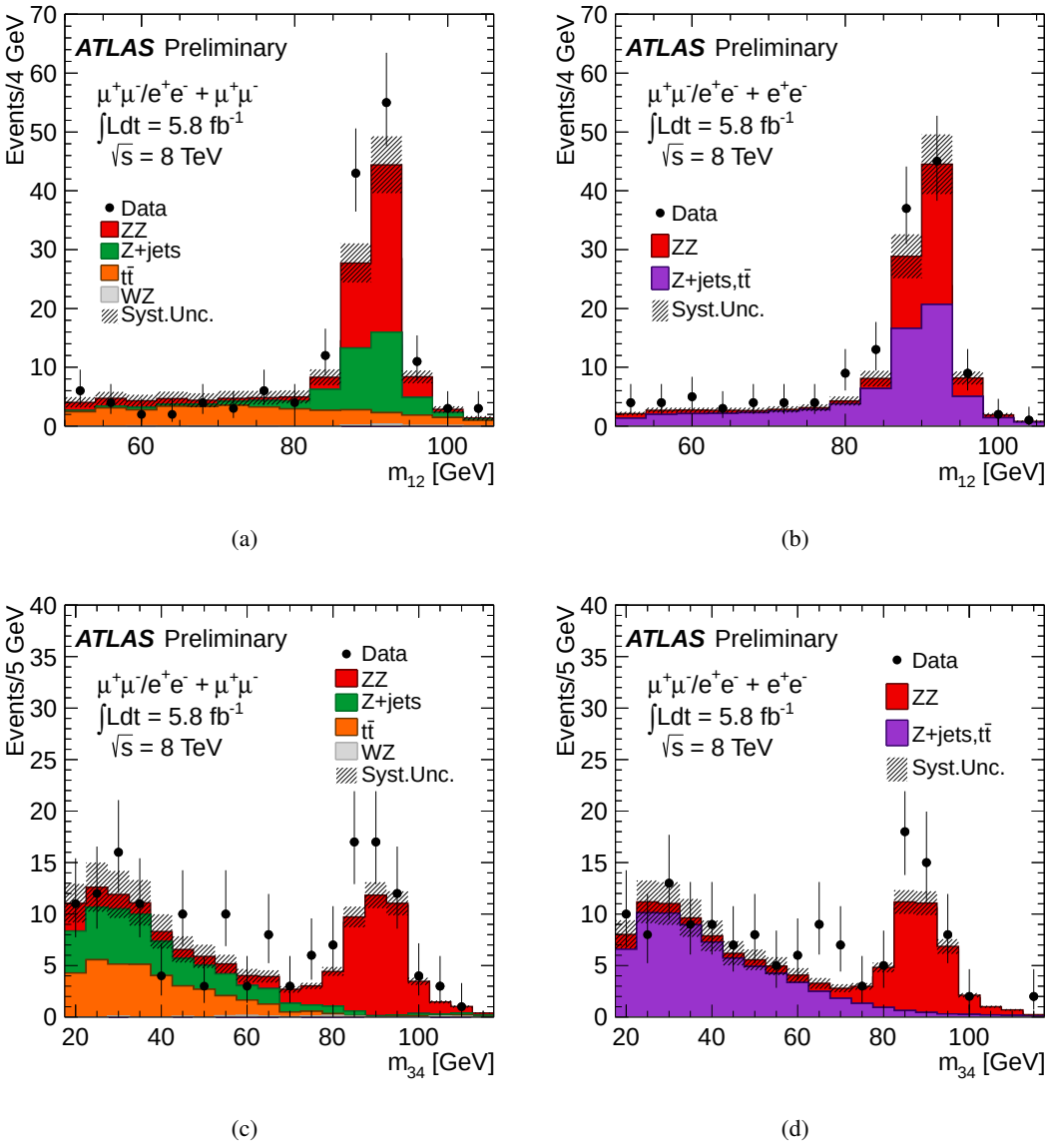

Figure 4: Invariant mass distributions of the lepton pairs in the control sample defined by a Z boson candidate and an additional same-flavour lepton pair, for the $\sqrt{s} = 8$ TeV dataset. The sample is divided according to the flavour of the additional lepton pair. In (a) the m_{12} and in (c) the m_{34} distributions are presented for $\ell\ell\,(\mu^+\mu^-/e^+e^-) + \mu^+\mu^-$ events. In (b) the m_{12} and in (d) the m_{34} distributions are presented for $\ell\ell\,(\mu^+\mu^-/e^+e^-) + e^+e^-$ events. The kinematic selection of the analysis is applied. Isolation and impact parameter significance requirements are applied to the first lepton pair only. The MC is normalized to the data driven background estimations given in Table 4.

5 Analysis of $\sqrt{s} = 7$ TeV data

In this section the analysis of the 2011 $\sqrt{s} = 7$ TeV data, using the same kinematic selection as the $\sqrt{s} = 8$ TeV analysis, is presented.

The data collected during 2011 are subjected to quality requirements similar to those used for the 2012 data. The resulting integrated luminosity being 4.8 fb^{-1}, 4.8 fb^{-1} and 4.9 fb^{-1} for the 4μ, $2e2\mu/2\mu2e$ and $4e$ final states, respectively.

5.1 Lepton Reconstruction/Identification and Event Selection

The data considered in this analysis are selected using single-lepton or di-lepton triggers. For the single-muon trigger the p_{T} threshold is 18 GeV, while for the single-electron trigger the E_{T} threshold is $20 - 22$ GeV depending on the LHC data-taking period. For the di-muon and di-electron triggers the thresholds are $p_{\mathrm{T}} = 10$ GeV for each muon, and $E_{\mathrm{T}} = 12$ GeV for both electrons.

For the $\sqrt{s} = 7$ TeV dataset, the electron reconstruction proceeds as described in Ref. [70], with the exception that electron candidates are refitted using a Gaussian-sum filter [73], which recovers electron candidates that suffered large energy losses due to bremsstrahlung emissions. Electron reconstruction and identification is similar to that used in Ref. [6].

The event selection is identical between $\sqrt{s} = 7$ TeV and 8 TeV data analyses with the following exceptions:

- For the electron track isolation, tracks are required to have at least seven silicon hits, one b-layer hit and $p_{\mathrm{T}} > 1$ GeV.
- The calorimeter isolation of electrons in 2011 is cell-based rather than topological cluster based and the actual cut is 0.3 instead of 0.2.

The combined signal reconstruction and selection efficiency for $m_H = 130$ GeV ($m_H = 360$ GeV) is 43% (70%) for the 4μ channel, 23% (56%) for the $2e2\mu/2\mu2e$ channel and 17% (45%) for the $4e$ channel.

5.2 Background Estimation

The background estimation strategy in the $\sqrt{s} = 7$ TeV data sample is identical to the $\sqrt{s} = 8$ TeV one, described in Section 4.2.

The estimation of the $t\bar{t}$ and Z + jets (dominated by $Zb\bar{b}$) background events in the signal region using the fit in m_{12}, described in Section 4.2.1, is shown in Fig. 5. For the $e^{\pm}\mu^{\mp} + \mu^{+}\mu^{-}$ control region 8 events are observed in data with 11.0 ± 0.6 expected from MC. For the $\ell\ell + ee$ control region (defined in Section 4.2.2), the number of events observed in the dataset from $\sqrt{s} = 7$ TeV in each category of the control region are summarised in Table 5. The final expectations in the signal region are summarised in Table 6.

The $\ell\ell + ee$ background estimate from performing the full analysis but selecting same-sign pairs for the sub-leading di-electrons gives 4 (1) events below $m_{4\ell} = 160$ GeV in the $4e$ ($2\mu2e$) sub-channel.

Figure 6 displays the invariant masses of lepton pairs in events with a Z boson candidate and an additional same-flavour lepton pair, selected by applying the kinematic requirements of the analysis, and by applying isolation requirements to the first lepton pair only. The events are divided according to the flavour of the additional lepton pair into $\ell\ell + \mu\mu$ and $\ell\ell + ee$ samples. In Figs. 6(a) and 6(c) the m_{12} and m_{34} distributions are presented for $\ell\ell + \mu\mu$ events, while in Figs. 6(b) and 6(d) the corresponding distributions are presented for $\ell\ell + ee$ events. The shape and normalisation of the backgrounds discussed earlier are in good agreement with data; this is observed both for large values of m_{34}, where the $ZZ^{(*)}$ background dominates, and for low m_{34} values.

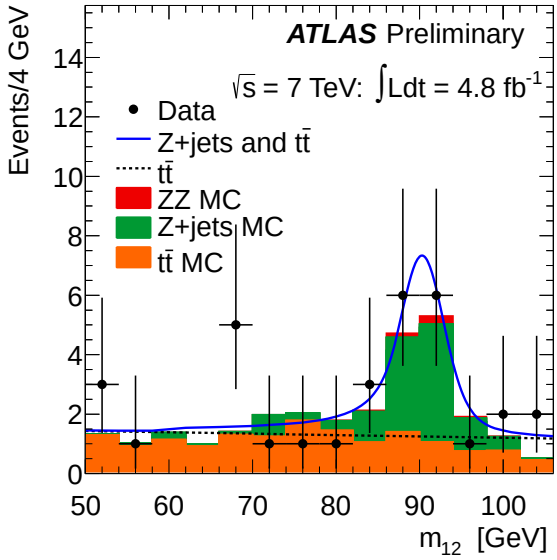

Figure 5: Distribution of m_{12}, for $\sqrt{s} = 7$ TeV, in the control region where the isolation requirements are not applied to the two sub-leading muons, and at least one of these muons fails the impact parameter significance requirement. The fit used to obtain the yields for $t\bar{t}$ and Z + jets is presented, the MC expectations are also shown for comparison.

Table 5: The observed yields of the various categories in the $\ell\ell + ee$ control region for $\sqrt{s} = 7$ TeV. Events are classified according to whether the electron candidates of the sub-leading di-electrons are: electron-like (E), conversion-like (C) and fake-like (F). For comparison the MC expectations are also shown. The di-lepton categorization in reconstruction categories is ordered in p_{T}.

	$4e$		$2\mu 2e$	
	Data	MC	Data	MC
EE	11	11.2±0.6	8	15.0±0.9
EC	4	2.5±0.8	3	3.0±1.1
EF	6	9.7±1.4	5	6.6±1.1
CE	5	1.5±0.7	6	4.5±1.6
CC	2	1.4±0.7	2	1.5±1.0
CF	7	4.7±1.2	10	9.9±2.3
FE	5	3.1±0.6	4	4.5±1.0
FC	5	3.0±1.0	4	6.3±1.8
FF	12	11.0±1.9	17	13.4±2.6
Total	57	48±3	59	65±5

Table 6: Summary of the background estimates for the $\sqrt{s} = 7$ TeV data sample. The "†" symbol indicates the estimated number of events used for the background normalisation, the others being cross-checks. The first uncertainty is statistical, while the second is systematic.

Method	Estimated number of events
4μ	
m_{12} fit: Z + jets contribution	$0.25\pm 0.10 \pm 0.08^{\dagger}$
m_{12} fit: $t\bar{t}$ contribution	$0.022\pm 0.010\pm 0.011^{\dagger}$
$t\bar{t}$ from $e^{\pm}\mu^{\mp} + \mu^{\pm}\mu^{\mp}$	$0.025\pm 0.009\pm 0.014$
$2e2\mu$	
m_{12} fit: Z + jets contribution	$0.20\pm 0.08 \pm 0.06^{\dagger}$
m_{12} fit: $t\bar{t}$ contribution	$0.020\pm 0.009\pm 0.011^{\dagger}$
$t\bar{t}$ from $e^{\pm}\mu^{\mp} + \mu^{\pm}\mu^{\mp}$	$0.024\pm 0.009\pm 0.014$
$2\mu 2e$	
$\ell\ell + e^{\pm}e^{\mp}$	$2.6\pm 0.4 \pm 0.4^{\dagger}$
$\ell\ell + e^{\pm}e^{\pm}$	$3.7\pm 0.9 \pm 0.6$
$3\ell + \ell$ (same-sign)	$2.0\pm 0.5 \pm 0.3$
$4e$	
$\ell\ell + e^{\pm}e^{\mp}$	$3.1\pm 0.6 \pm 0.5^{\dagger}$
$\ell\ell + e^{\pm}e^{\pm}$	$3.2\pm 0.6 \pm 0.5$
$3\ell + \ell$ (same-sign)	$2.2\pm 0.5 \pm 0.3$

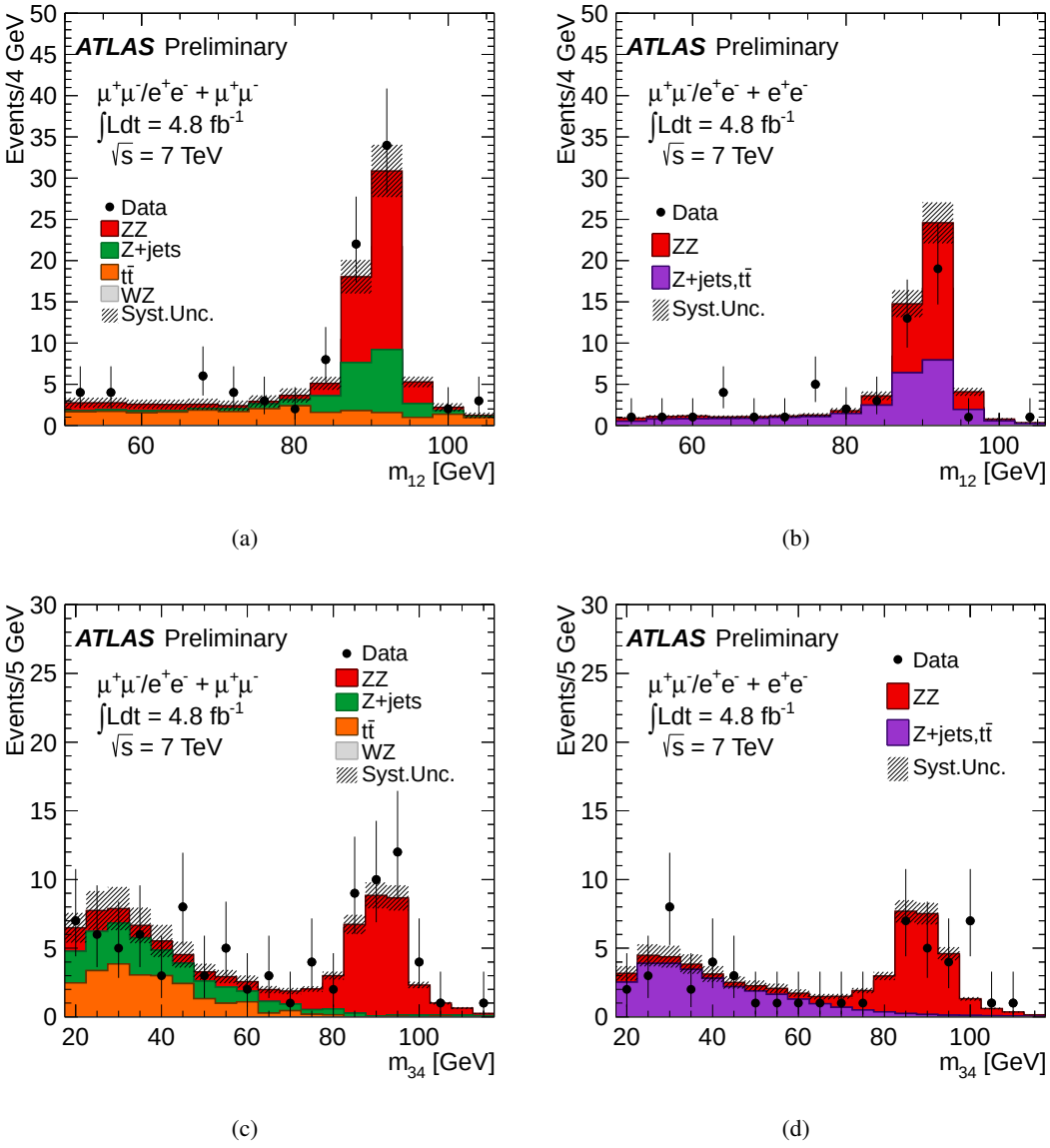

Figure 6: Invariant mass distributions of the lepton pairs in the control sample defined by a Z boson candidate and an additional same-flavour lepton pair for the $\sqrt{s} = 7$ TeV data sample. The sample is divided according to the flavour of the additional lepton pair. In (a) the m_{12} and in (c) the m_{34} distributions are presented for $\ell\ell\,(\mu^+\mu^-/e^+e^-) + \mu^+\mu^-$ events. In (b) the m_{12} and in (d) the m_{34} distributions are presented for $\ell\ell\,(\mu^+\mu^-/e^+e^-) + e^+e^-$ events. The kinematic selections of the analysis are applied. Isolation requirements are applied to the first lepton pair only. The MC is normalized to the data driven background estimations given in Table 6.

6 Systematic Uncertainties

The uncertainty of the lepton reconstruction and identification efficiencies, and of the momentum resolution and scale, are determined using samples of W, Z and J/ψ decays [70]. The uncertainty of the muon identification and reconstruction efficiency results in a relative acceptance uncertainty of the signal and the $ZZ^{(*)}$ background which is uniform over the mass range of interest, and amounts to ±0.16% (±0.12%) for the 4μ ($2e2\mu$) channel. The uncertainty of the electron identification efficiency results in a relative acceptance uncertainty of ± 3.0% (±1.7%) for the $4e$ ($2e2\mu$) channel at $m_{4\ell} = 600$ GeV and reaches ±8.0% (±4.6%) at $m_{4\ell} = 110$ GeV. The effects of muon momentum resolution and scale uncertainty are found to be negligible. The effect of the uncertainty of the energy resolution for electrons is negligible, while the uncertainty of the electron energy scale results in an uncertainty of less than ±0.7% (±0.4%) on the mass scale of the $m_{4\ell}$ distribution for the $4e$ ($2e2\mu$) channel.

The selection efficiency of the isolation and impact parameter requirements is studied using data for both isolated and non-isolated leptons. Isolated leptons are obtained from $Z \to \ell\ell$ decays, while additional leptons reconstructed in events with $Z \to \ell\ell$ decays constitute the sample of non-isolated leptons. Additional checks are performed with non-isolated leptons from semi-leptonic b- and c-quark decays in a heavy-flavour enriched di-jet sample. Good agreement is observed between data and simulation and the systematic uncertainty is, in general, estimated to be small with respect to the other systematic uncertainties.

An additional uncertainty on the signal selection efficiency is added in the 2011 analysis only, which is not needed in the 2012 analysis due to an improved modelling of the signal kinematics. This additional uncertainty is evaluated by varying the Higgs boson p_{T} spectrum in the gluon fusion process according to the PDF and QCD scale uncertainties.

The background uncertainties of the data driven methods have already been presented in Sections 4 and 5. The overall uncertainty of the integrated luminosity for the complete 2011 dataset is ±1.8% and is described in Refs. [10, 11]. For the 2012 dataset the corresponding preliminary uncertainty is ±3.6% based on the calibration described in Ref. [11].

The theory-related systematic uncertainty, for both signal and $ZZ^{(*)}$ background, has been discussed in Section 3. The uncertainties related to the data-driven methods are summarised in Tables 4 and 6.

7 Results

In Table 7, the numbers of events observed in each final state are summarised and compared to the expected backgrounds, separately for $m_{4\ell} < 160$ GeV and $m_{4\ell} \geq 160$ GeV, and to the expected signal for various m_H hypotheses. Table 8 presents the observed and expected events, in a window of ±5 GeV around various hypothesized Higgs boson masses, for the 5.8 fb^{-1} at $\sqrt{s} = 8$ TeV and the 4.8 fb^{-1} at $\sqrt{s} = 7$ TeV datasets as well as for their combination.

The expected $m_{4\ell}$ distributions for the total background and several signal hypotheses are compared to the data in Fig. 7. Figure 8 presents the same distributions only for the low mass range 80–250 GeV. In Figures 9 and 10 the $m_{4\ell}$ mass distributions for each sub-channel (4μ, $2\mu2e$, $2e2\mu$, $4e$) are shown for the data at $\sqrt{s} = 8$ TeV and $\sqrt{s} = 7$ TeV, respectively. High-p_{T} photon emissions from final-state radiation (FSR), although occurring at a low rate, are not taken into account explicitely in the lepton reconstruction, and affect the reconstructed invariant mass in rare cases. In MC, QED corrections are fully considered and accounted for in the templates used for the mass distributions. All candidates selected have been checked and no appreciable FSR activity has been found for the candidates below 160 GeV.

Upper limits are set on the Higgs boson production cross section at 95% CL, using the CL_s modified frequentist formalism [74] with the profile likelihood ratio test statistic [75]. The test statistic is evaluated using a maximum-likelihood fit of signal and background models to the observed $m_{4\ell}$ distribution.

Table 7: The observed numbers of events and the final estimate for the expected backgrounds, separated into "Low mass" ($m_{4\ell} < 160$ GeV) and "High mass" ($m_{4\ell} \geq 160$ GeV) regions. The expected numbers of signal events is also shown for various Higgs boson mass hypotheses. For signal and background estimates, the corresponding total uncertainty is given.

	4μ		$2e2\mu/2\mu2e$		$4e$	
	Low mass	High mass	Low mass	High mass	Low mass	High mass
$\sqrt{s} = 8$ TeV						
Int. Luminosity	5.8 fb^{-1}		5.8 fb^{-1}		5.9 fb^{-1}	
$ZZ^{(*)}$	6.3±0.3	27.5±1.9	3.7±0.2	41.7±3.0	2.9±0.3	17.7±1.4
Z + jets, and $t\bar{t}$	0.4±0.2	0.15±0.07	3.9±0.9	1.4±0.3	2.9±0.8	1.0±0.3
Total Background	6.7±0.3	27.6±1.9	7.6±1.0	43.1±3.0	5.7±0.8	18.8±1.4
Data	4	34	11	61	7	25
$m_H = 125$ GeV	1.4±0.2		1.7±0.2		0.8±0.1	
$m_H = 150$ GeV	4.5±0.6		5.9±0.8		2.7±0.4	
$m_H = 190$ GeV	8.2±1.0		12.5±1.7		5.3±0.8	
$m_H = 400$ GeV	3.9±0.5		6.6±0.9		2.9±0.4	
$\sqrt{s} = 7$ TeV						
Int. Luminosity	4.8 fb^{-1}		4.8 fb^{-1}		4.9 fb^{-1}	
$ZZ^{(*)}$	4.9±0.2	18.1±1.3	3.1±0.2	27.3±2.0	1.6±0.2	10.2±0.8
Z + jets, and $t\bar{t}$	0.2±0.1	0.07±0.03	2.1±0.5	0.7±0.2	2.3±0.6	0.8±0.2
Total Background	5.1±0.2	18.2±1.3	5.1±0.5	28.0±2.0	3.9±0.6	11.0±0.8
Data	8	25	5	28	4	18
$m_H = 125$ GeV	1.0±0.1		1.0±0.1		0.37±0.05	
$m_H = 150$ GeV	3.0±0.4		3.4±0.5		1.4±0.2	
$m_H = 190$ GeV	5.1±0.6		7.4±1.0		2.8±0.4	
$m_H = 400$ GeV	2.3±0.3		3.8±0.5		1.6±0.2	

Table 8: The numbers of expected signal and background events together with the number of observed events, in a window of ±5 GeV around the hypothesized Higgs boson mass for the 5.8 fb^{-1}at $\sqrt{s} = 8$ TeV and the 4.8 fb^{-1}at $\sqrt{s} = 7$ TeV datasets as well as for their combination.

	$\sqrt{s} = 8$ TeV			$\sqrt{s} = 7$ TeV			$\sqrt{s} = 8$ TeV and $\sqrt{s} = 7$ TeV		
				4μ					
m_H	exp. signal	exp. bkg	obs	exp. signal	exp. bkg	obs	exp. signal	exp. bkg	obs
120	0.68±0.09	0.61± 0.04	2	0.48±0.06	0.46± 0.03	2	1.16± 0.15	1.07± 0.07	4
125	1.25±0.17	0.74± 0.05	4	0.84±0.11	0.56± 0.03	2	2.09± 0.28	1.30± 0.08	6
130	1.88±0.25	0.81± 0.05	2	1.38±0.18	0.63± 0.03	1	3.26± 0.43	1.44± 0.08	3
				$2e2\mu/2\mu2e$					
m_H	exp. signal	exp. bkg	obs	exp. signal	exp. bkg	obs	exp. signal	exp. bkg	obs
120	0.81±0.12	1.15± 0.17	2	0.48±0.07	0.78± 0.10	1	1.29± 0.19	1.93± 0.18	3
125	1.45±0.20	1.30± 0.19	3	0.83±0.11	0.89± 0.11	2	2.28± 0.31	2.19± 0.21	5
130	2.24±0.32	1.34± 0.20	2	1.27±0.17	0.94± 0.11	1	3.51± 0.49	2.28± 0.21	3
				$4e$					
m_H	exp. signal	exp. bkg	obs	exp. signal	exp. bkg	obs	exp. signal	exp. bkg	obs
120	0.35±0.05	0.79±0.15	1	0.15±0.02	0.60±0.12	1	0.50±0.07	1.39±0.19	2
125	0.61±0.09	0.90±0.17	2	0.28±0.04	0.69±0.13	0	0.89±0.13	1.59±0.22	2
130	0.91±0.15	0.96±0.17	1	0.42±0.06	0.74±0.14	0	1.33±0.21	1.70±0.22	1

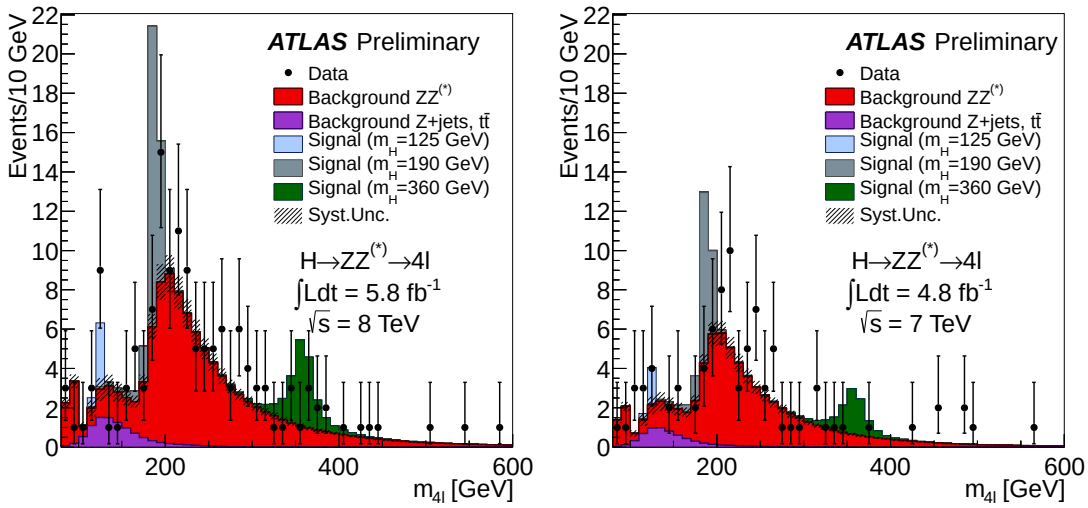

(a) (b)

Figure 7: The distribution of the four-lepton invariant mass, $m_{4\ell}$, for the selected candidates compared to the background expectation in the range 80−600 GeV for the (a) $\sqrt{s} = 8$ TeV8 and (b) $\sqrt{s} = 7$ TeV datasets. The error bars represent the 68.3% central confidence intervals. The signal expectation for several m_H hypotheses is also shown. The resolution of the reconstructed Higgs boson mass is dominated by detector resolution at low m_H values and by the Higgs boson width at high m_H.

Figures 11, 12 and 13 show the observed and expected 95% CL cross section upper limits, as a function of m_H, for the $\sqrt{s} = 8$ TeV data, the $\sqrt{s} = 7$ TeV data and for the combination of the two datasets. Combining the two datasets, the SM Higgs boson is excluded at 95% CL in the mass ranges 131−162 GeV and 170−460 GeV. The expected exclusion ranges are 124−164 GeV and 176−500 GeV.

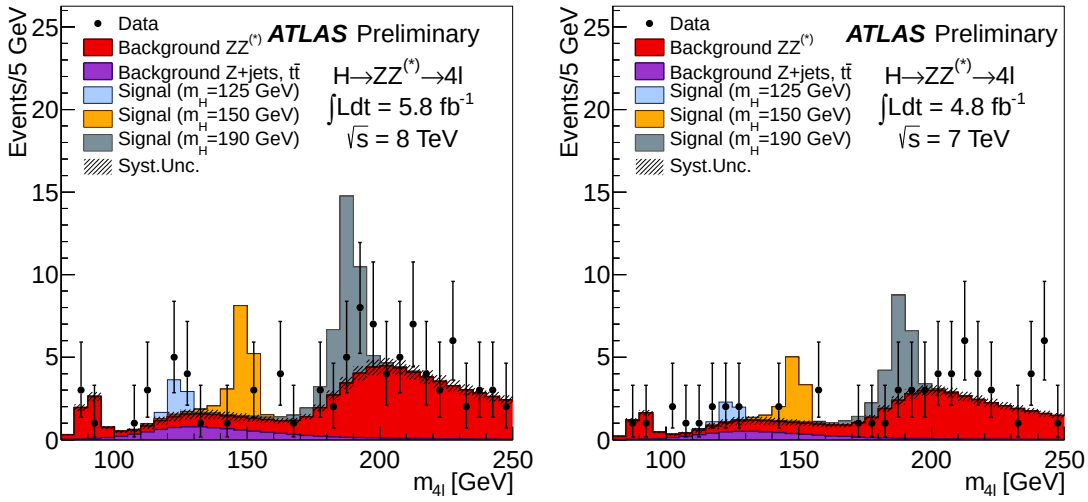

(a) (b)

Figure 8: The distribution of the four-lepton invariant mass, $m_{4\ell}$, for the selected candidates compared to the background expectation in the 80−250 GeV mass range for the (a) $\sqrt{s} = 8$ TeV and (b) $\sqrt{s} = 7$ TeV datasets. Error bars represent 68.3% central confidence intervals. The signal expectation for several m_H hypotheses is also shown.

The significance of an excess is given by the probability, p_0, that a background-only experiment is more signal-like in terms of the test statistic than the observed data. In Figure 14 the local p_0, obtained using the asymptotic approximation of Ref. [75], is presented as a function of the m_H hypothesis for the combination of $\sqrt{s} = 8$ and 7 TeV data samples. For comparison the results for the two data samples are given separately in Fig. 15.

The most significant upward deviations from the background-only hypothesis in the $\sqrt{s} = 7$ TeV data are observed for $m_H = 242$ GeV with a local p_0 of 0.5% (2.6 standard deviations), and for $m_H = 125$ GeV with a local p_0 of 1.1% (2.3 standard deviations). In the $\sqrt{s} = 8$ TeV data, they are at $m_H = 125.5$ GeV with a local p_0 of 0.4% (2.7 standard deviations), and for $m_H = 266$ GeV with a local p_0 of 3.5% (1.8 standard deviations). In the combined analysis of the two datasets, the lowest local p_0 value is 0.029% (3.4 standard deviations), at $m_H = 125$ GeV. The probability that such an excess occurs anywhere in the full mass range considered in this search (*i.e.*, the *look-elsewhere effect* on the above p_0 value), is evaluated using the method of Ref. [76], using the mass range between 110 GeV and 141 GeV (*i.e.*, the mass range not previously excluded at the 95% C.L. by the LHC experiments [77]). The *global* p_0 of the excess located at $m_H = 125$ GeV is 0.65%, or 2.5 standard deviations. In the high mass region ($m_H > 160$ GeV), the lowest p_0 is at 1.9% (2.1 standard deviations), at $m_H = 266$ GeV.

To determine the potential effect on the p_0 due to the SM $ZZ^{(*)}$ production normalisation, a test is performed where the $ZZ^{(*)}$ normalisation is obtained directly from the data. No significant modification of the observed and expected p_0 in the low m_H region is observed.

In Fig. 16(a) the signal strength parameter $\mu = \sigma/\sigma_{SM}$ is presented as a function of m_H for the combination of the two data samples. The corresponding result in the case where a SM Higgs signal of $m_H = 125$ GeV is injected is shown in Fig. 16(b). The bands illustrate the μ interval corresponding to $-2\ln\lambda(\mu) < 1$, where λ is the profile likelihood ratio test statistic, and represent an approximate $\pm 1\sigma$ variation. The fitted signal strength divided by the expected SM rate is denoted with $\hat{\mu}$. The expected $\hat{\mu}$ has an asymmetric shape and because the expected SM rate rises rapidly with m_H in the low mass region, the expected $\hat{\mu}$ is increased below the injected signal mass and slightly exceeds one for a small mass

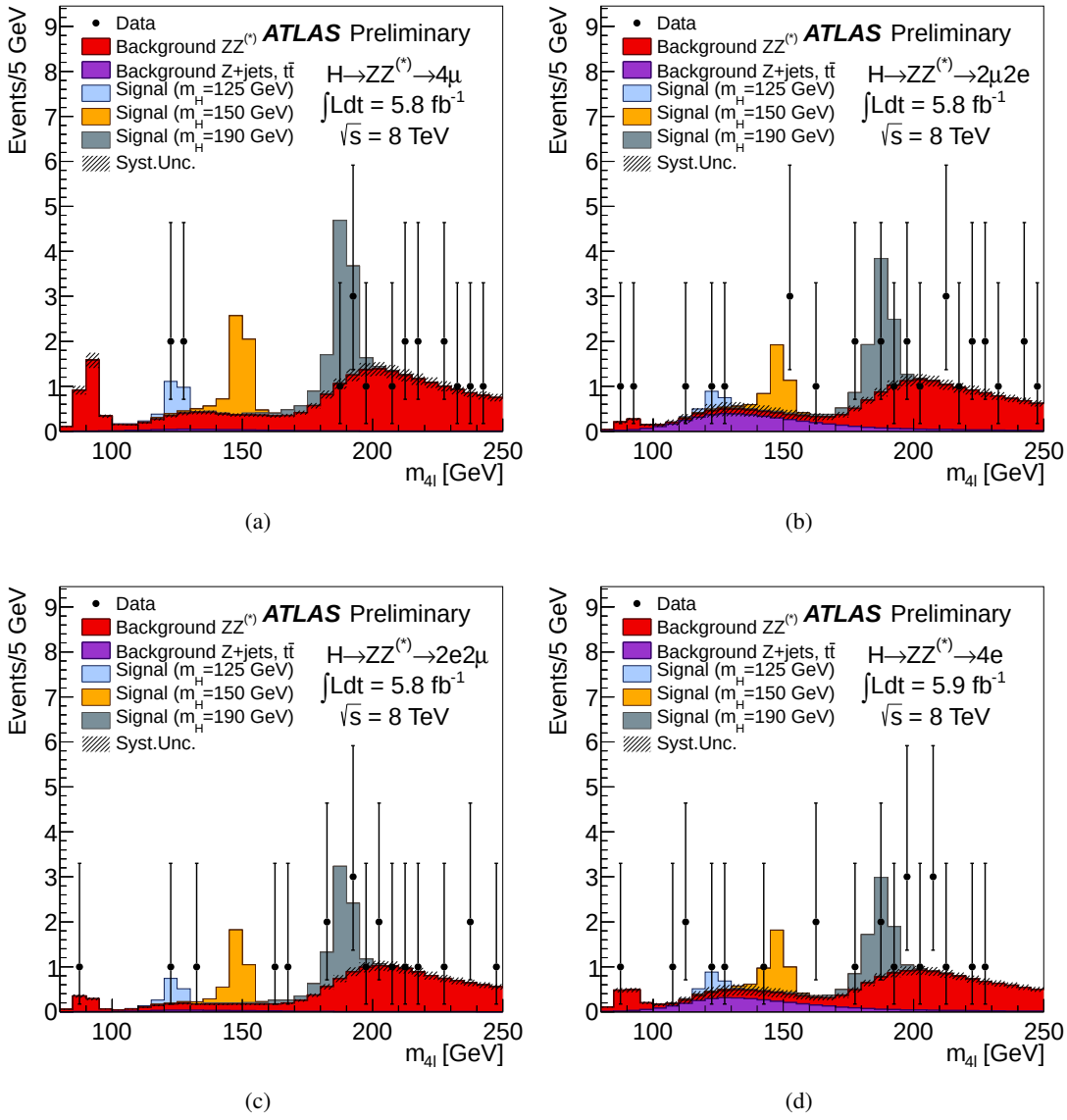

Figure 9: The distribution of the four-lepton invariant mass, $m_{4\ell}$, for the selected candidates for the $\sqrt{s} = 8$ TeV analysis, for the various sub-channels (a) 4μ , (b) $2\mu 2e$, (c) $2e2\mu$, (d) $4e$, compared to the background expectation for the 80−250 GeV mass range. Error bars represent 68.3% central confidence intervals. The signal expectation for several m_H hypotheses is also shown.

range.

Figure 17 presents the best μ and m_H fit and the profile likelihood ratio contours that, in the asymptotic limit, would correspond to 68% and 95% confidence levels.

8 Summary

A search for the SM Higgs boson in the decay channel $H \to ZZ^{(*)} \to 4\ell$ based on 4.8 fb^{-1} of data recorded with the ATLAS detector at $\sqrt{s} = 7$ TeV during 2011 and 5.8 fb^{-1} recorded at $\sqrt{s} = 8$ TeV during 2012 has been presented. The SM Higgs boson is excluded at 95% CL in the mass ranges 131−162 GeV and 170−460 GeV. An excess of events is observed around $m_H = 125$ GeV, whose p_0 value is

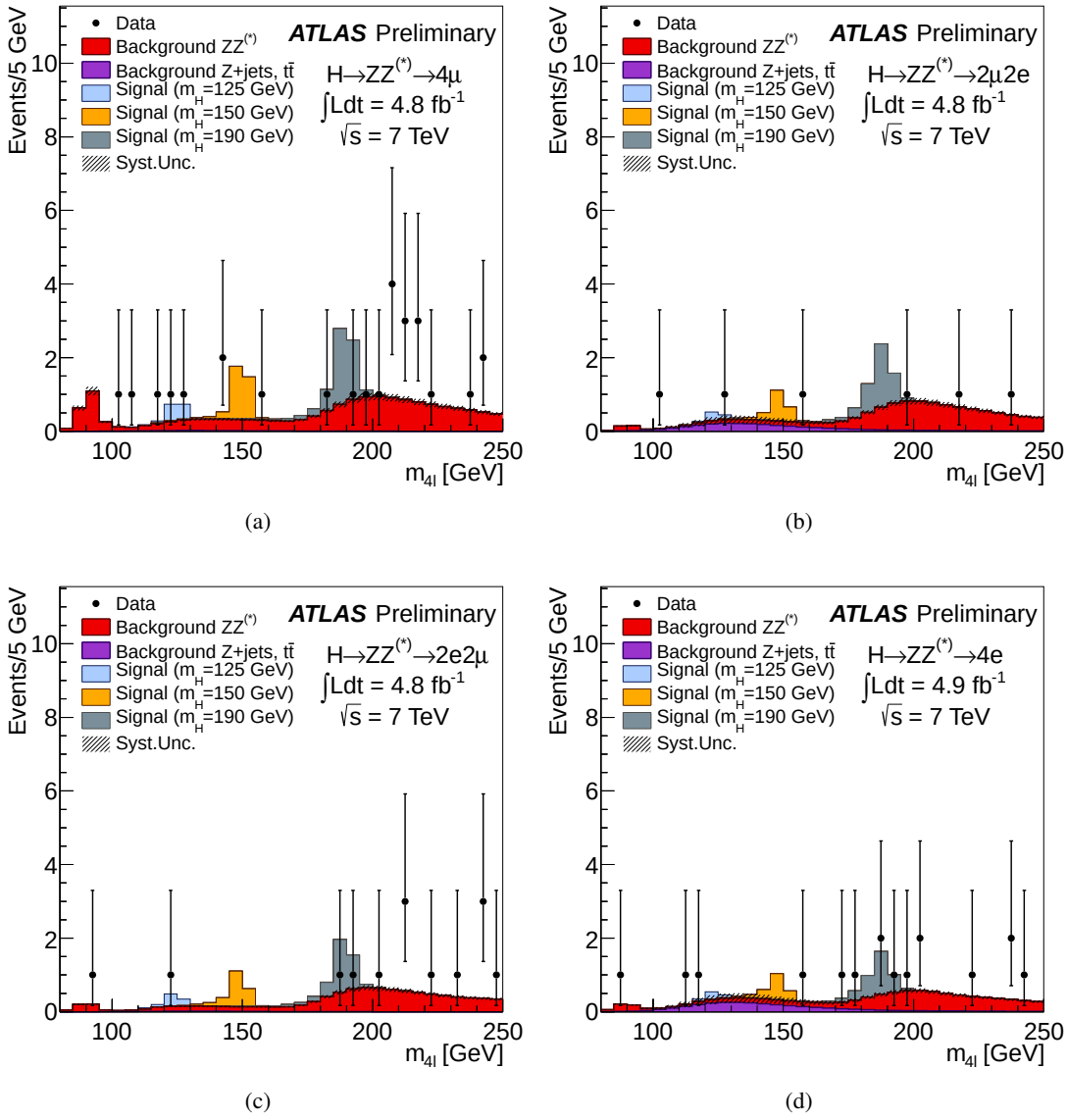

Figure 10: The distribution of the four-lepton invariant mass, $m_{4\ell}$, for the selected candidates for the $\sqrt{s}$ = 7 TeV analysis for the various sub-channels (a) 4μ , (b) $2\mu 2e$, (c) $2e2\mu$, (d) $4e$, compared to the background expectation for the 80−250 GeV mass range. Error bars represent 68.3% central confidence intervals. The signal expectation for several m_H hypotheses is also shown.

0.029% (3.4 standard deviations) in the combined analysis of the two datasets.

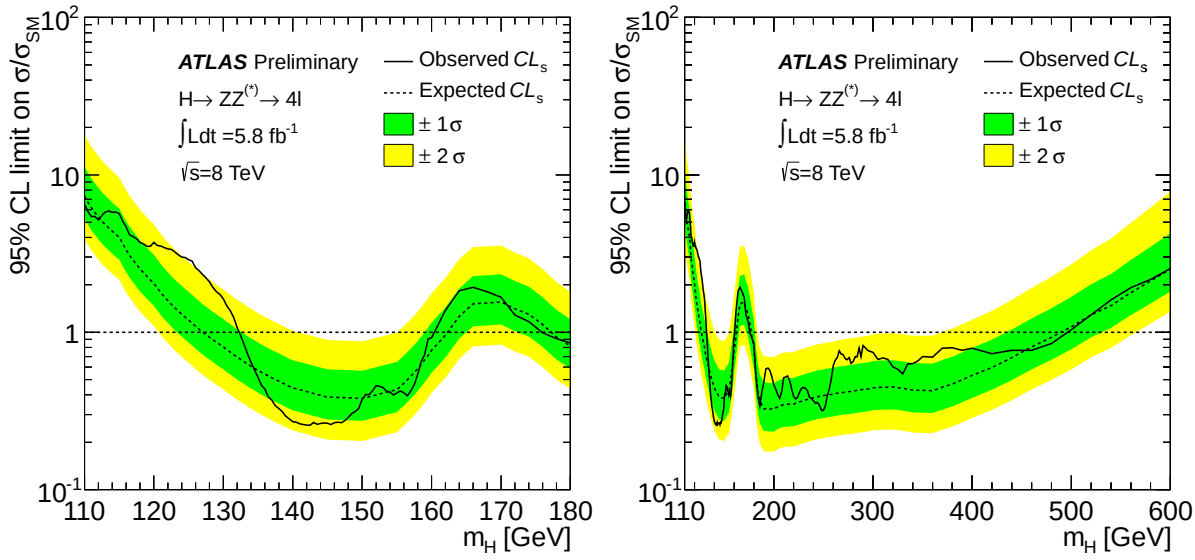

(a) (b)

Figure 11: The expected (dashed) and observed (full line) 95% CL upper limits on the Standard Model Higgs boson production cross section as a function of m_H, divided by the expected SM Higgs boson cross section, for the $\sqrt{s} = 8$ TeV data sample. The dark (green) and light (yellow) bands indicate the expected limits with $\pm 1\sigma$ and $\pm 2\sigma$ fluctuations, respectively; (a) shows the low mass range, and (b) the full range under consideration.

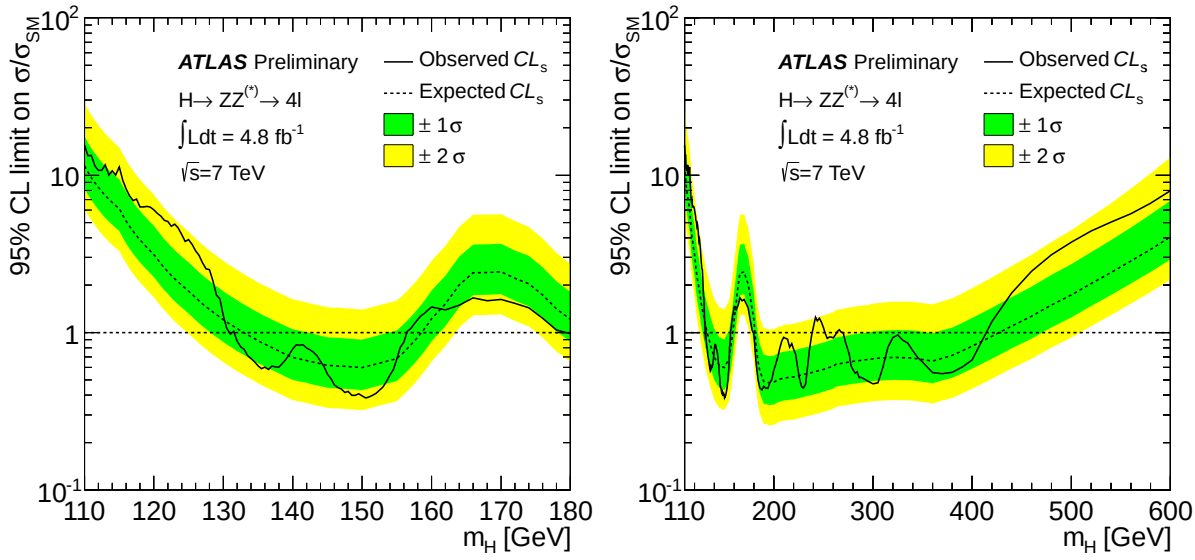

(a) (b)

Figure 12: The expected (dashed) and observed (full line) 95% CL upper limits on the SM Higgs boson production cross section as a function of m_H, divided by the expected SM Higgs boson cross section for the $\sqrt{s} = 7$ TeV data sample. The dark (green) and light (yellow) bands indicate the expected limits with $\pm 1\sigma$ and $\pm 2\sigma$ fluctuations, respectively; (a) shows the low mass range, and (b) the full range under consideration.

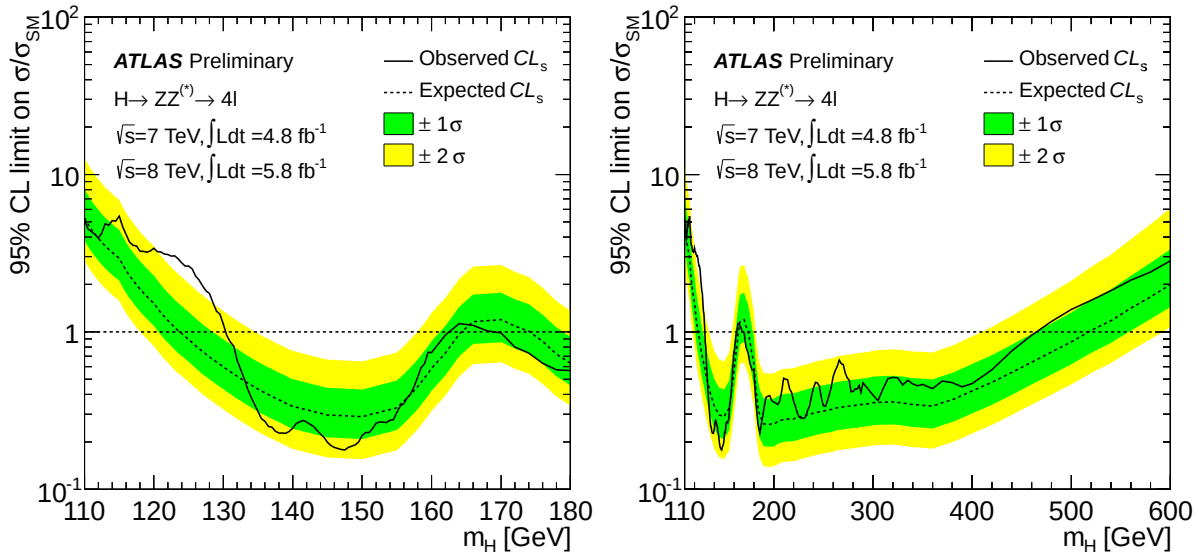

(a) (b)

Figure 13: The expected (dashed) and observed (full line) 95% CL upper limits on the Standard Model Higgs boson production cross section as a function of m_H, divided by the expected SM Higgs boson cross section, for the combination of the $\sqrt{s} = 7$ TeV and $\sqrt{s} = 8$ TeV data samples. The dark (green) and light (yellow) bands indicate the expected limits with $\pm 1\sigma$ and $\pm 2\sigma$ fluctuations, respectively; (a) shows the low mass range, and (b) the full range under consideration.

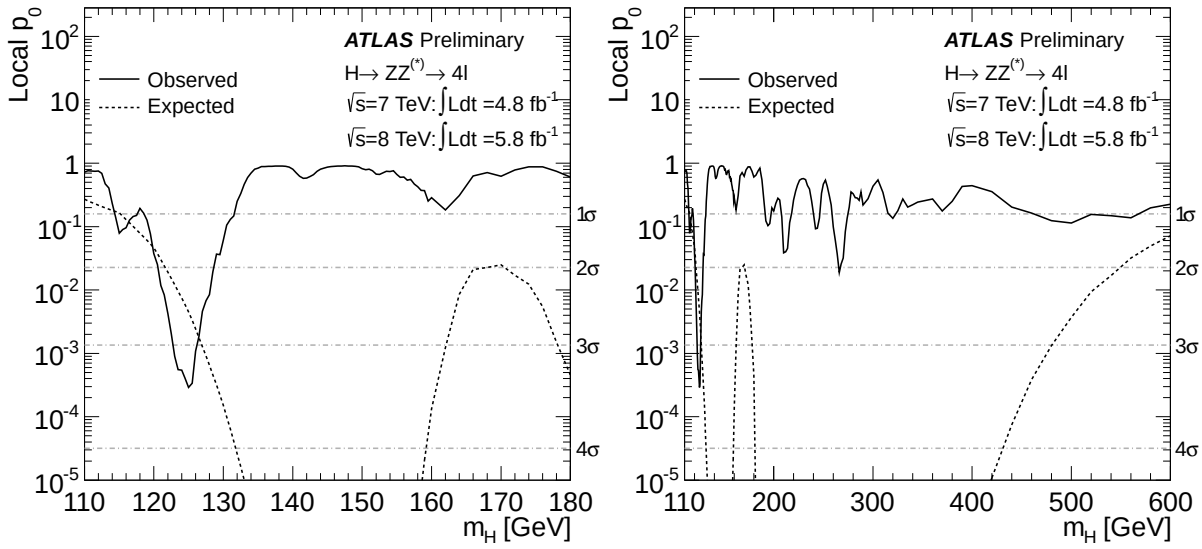

(a) (b)

Figure 14: The observed local p_0 for the combination of the 2011 and 2012 datasets (solid line). The dashed curve shows the expected median local p_0 for the signal hypothesis when tested at the corresponding m_H. The horizontal dashed lines indicate the p_0 values corresponding to local significances of 1σ, 2σ, 3σ and 4σ.

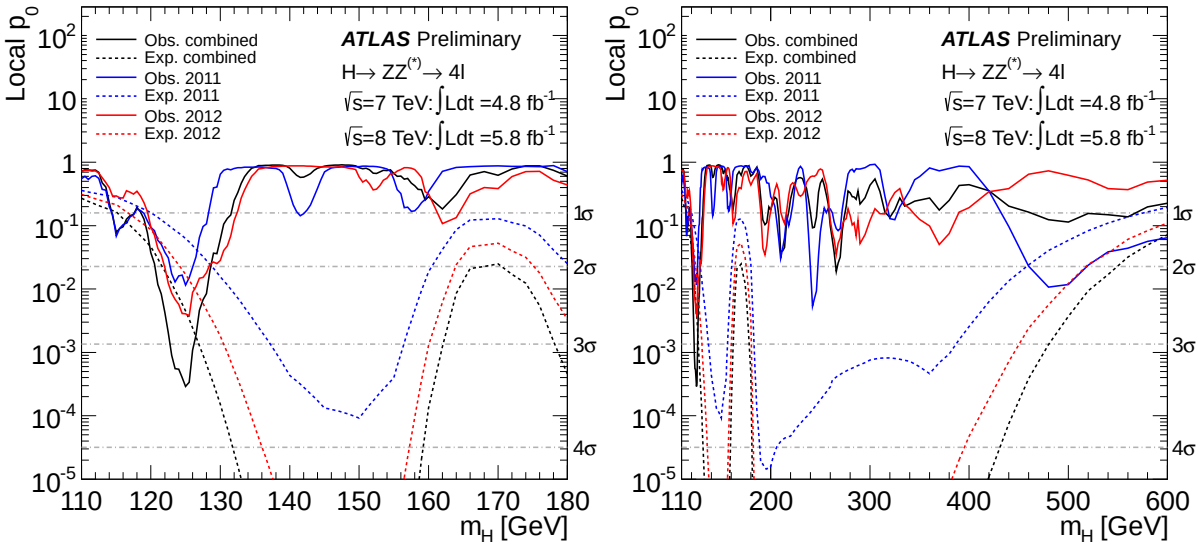

(a) (b)

Figure 15: The observed local p_0 for the combination of the 2011 and 2012 datasets (solid black line); the $\sqrt{s} = 7$ TeV and $\sqrt{s} = 8$ TeV data results are shown in solid lines (blue and red, respectively). The dashed curves show the expected median local p_0 for the signal hypothesis when tested at the corresponding m_H. The horizontal dashed lines indicate the p_0 values corresponding to local significances of 1σ, 2σ, 3σ and 4σ.

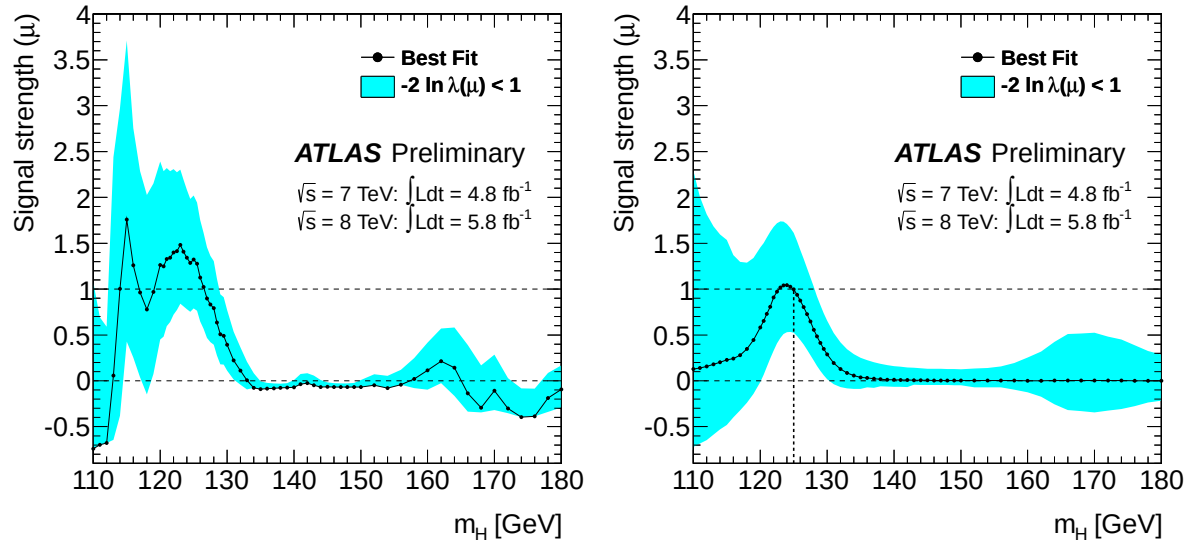

(a) (b)

Figure 16: The signal strength parameter $\mu = \sigma/\sigma_{SM}$ obtained from a fit to the data is presented (a) for the combined fit to the 2011 and 2012 data samples and (b) for the expected value of μ as a function of m_H when a SM Higgs signal with $m_H = 125$ GeV is injected.

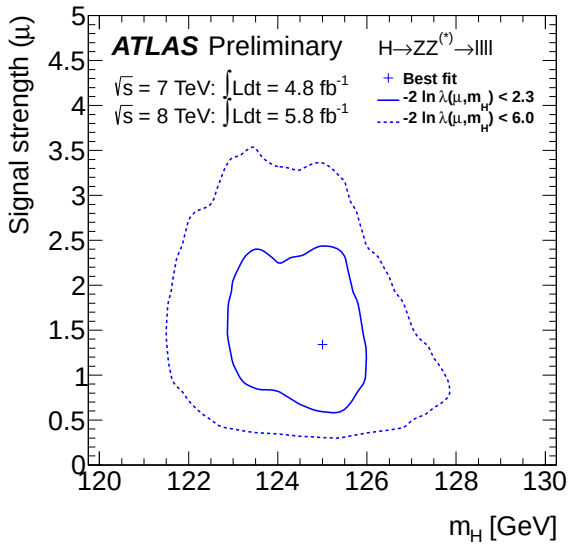

Figure 17: Best fit values for μ and m_H, and likelihood ratio contours that, in the asymptotic limit, correspond to 68% and 95% level contours in the (μ, m_H) plane.

References

[1] F. Englert and R. Brout, *Broken Symmetry and the Mass of Gauge Vector Mesons*, Phys. Rev. Lett. **13** (1964) 321–323.

[2] P. W. Higgs, *Broken Symmetries and the Masses of Gauge Bosons*, Phys. Rev. Lett. **13** (1964) 508–509.

[3] G. S. Guralnik, C. R. Hagen, and T. W. B. Kibble, *Global Conservation Laws and Massless Particles*, Phys. Rev. Lett. **13** (1964) 585–587.

[4] LEP Working Group for Higgs boson searches, ALEPH, DELPHI, L3 and OPAL Collaborations, *Search for the standard model Higgs boson at LEP*, Phys. Lett. **B 565** (2003) 61–75, arXiv:hep-ex/0306033.

[5] T. T. N. Physics and H. W. Group, *Combined CDF and D0 Search for Standard Model Higgs Boson Production with up to 10.0 fb^{-1} of Data*, 2012. arXiv:1203.3774 [hep-ex].

[6] ATLAS Collaboration, *Search for the Standard Model Higgs boson in the decay channel $H \to ZZ^{(*)} \to 4\ell$ with 4.8 fb^{-1} of pp collision data at $\sqrt{s} = 7$ TeV with ATLAS*, Phys. Lett. **B710** (2012) 383–402, arXiv:1202.1415 [hep-ex].

[7] ATLAS Collaboration, *Combined search for the Standard Model Higgs boson using up to 4.9 fb^{-1} of pp collision data at $\sqrt{s} = 7$ TeV with the ATLAS detector at the LHC*, Phys. Lett. **B710** (2012) 49–66, arXiv:1202.1408 [hep-ex].

[8] CMS Collaboration, *Search for the standard model Higgs boson in the decay channel H to ZZ to 4 leptons in pp collisions at $\sqrt{s} = 7$ TeV*, arXiv:1202.1997 [hep-ex].

[9] CMS Collaboration, *Combined results of searches for the standard model Higgs boson in pp collisions at $\sqrt{s} = 7$ TeV*, Phys. Lett. **B710** (2012) 26–48, arXiv:1202.1488 [hep-ex].

[10] ATLAS Collaboration, *Luminosity Determination in pp Collisions at $\sqrt{s} = 7$ TeV Using the ATLAS Detector at the LHC*, Eur. Phys. J. **C 71** (2011) 1630, arXiv:1101.2185 [hep-ex].

[11] ATLAS Collaboration, *Luminosity Determination in pp Collisions at $\sqrt{s} = 7$ TeV using the ATLAS Detector in 2011*, ATLAS-CONF-2011-116 (2012) .

[12] ATLAS Collaboration, *The ATLAS Experiment at the CERN Large Hadron Collider*, JINST **3** (2008) S08003.

[13] ATLAS Collaboration, *The ATLAS Inner Detector commissioning and calibration*, Eur. Phys. J. **C 70** (2010) 787–821, arXiv:1004.5293 [physics.ins-det].

[14] ATLAS Collaboration, *Readiness of the ATLAS Liquid Argon Calorimeter for LHC Collisions*, Eur. Phys. J. **C 70** (2010) 723–753, arXiv:0912.2642 [physics.ins-det].

[15] ATLAS Collaboration, *Readiness of the ATLAS Tile Calorimeter for LHC collisions*, Eur. Phys. J. **C 70** (2010) 1193–1236, arXiv:1007.5423 [physics.ins-det].

[16] ATLAS Collaboration, *Commissioning of the ATLAS Muon Spectrometer with Cosmic Rays*, Eur. Phys. J. **C 70** (2010) 875–916, arXiv:1006.4384 [physics.ins-det].

[17] ATLAS Collaboration, *Performance of the ATLAS Trigger System in 2010*, Eur. Phys. J. **C72** (2012) 1849, arXiv:1110.1530 [hep-ex].

[18] S. Alioli, P. Nason, C. Oleari, and E. Re, *NLO Higgs boson production via gluon fusion matched with shower in POWHEG*, JHEP **04** (2009) 002, arXiv:0812.0578 [hep-ph].

[19] P. Nason and C. Oleari, *NLO Higgs boson production via vector-boson fusion matched with shower in POWHEG*, JHEP **02** (2010) 037, arXiv:0911.5299 [hep-ph].

[20] D. de Florian, G. Ferrera, M. Grazzini, and D. Tommasini, *Transverse-momentum resummation: Higgs boson production at the Tevatron and the LHC*, JHEP **11** (2011) 064, arXiv:1109.2109 [hep-ph].

[21] T. Sjostrand, S. Mrenna, and P. Z. Skands, *PYTHIA 6.4 Physics and Manual*, JHEP **05** (2006) 026, arXiv:hep-ph/0603175.

[22] T. Sjostrand, S. Mrenna, and P. Z. Skands, *A Brief Introduction to PYTHIA 8.1*, Comput. Phys. Commun. **178** (2008) 852–867, arXiv:0710.3820 [hep-ph].

[23] P. Golonka and Z. Was, *PHOTOS Monte Carlo: A Precision tool for QED corrections in Z and W decays*, Eur. Phys. J. **C 45** (2006) 97–107, arXiv:hep-ph/0506026.

[24] N. Davidson, T. Przedzinski, and Z. Was, *PHOTOS Interface in C++: Technical and Physics Documentation*, arXiv:1011.0937 [hep-ph].

[25] LHC Higgs Cross Section Working Group, S. Dittmaier, C. Mariotti, G. Passarino, and R. Tanaka (Eds.), *Handbook of LHC Higgs cross sections: 1. Inclusive observables*, 2011. arXiv:1101.0593 [hep-ph]. CERN-2011-002.

[26] LHC Higgs Cross Section Working Group, S. Dittmaier, C. Mariotti, G. Passarino, and R. Tanaka (Eds.), *Handbook of LHC Higgs Cross Sections: 2. Differential distributions*, 2012. arXiv:1201.3084 [hep-ph].

[27] A. Djouadi, M. Spira, and P. M. Zerwas, *Production of Higgs bosons in proton colliders: QCD corrections*, Phys. Lett. **B 264** (1991) 440–446.

[28] S. Dawson, *Radiative corrections to Higgs boson production*, Nucl. Phys. **B 359** (1991) 283–300.

[29] M. Spira, A. Djouadi, D. Graudenz, and P. M. Zerwas, *Higgs boson production at the LHC*, Nucl. Phys. **B 453** (1995) 17–82, arXiv:hep-ph/9504378.

[30] R. V. Harlander and W. B. Kilgore, *Next-to-next-to-leading order Higgs production at hadron colliders*, Phys. Rev. Lett. **88** (2002) 201801, arXiv:hep-ph/0201206.

[31] C. Anastasiou and K. Melnikov, *Higgs boson production at hadron colliders in NNLO QCD*, Nucl. Phys. **B 646** (2002) 220–256, arXiv:hep-ph/0207004.

[32] V. Ravindran, J. Smith, and W. L. van Neerven, *NNLO corrections to the total cross section for Higgs boson production in hadron hadron collisions*, Nucl. Phys. **B 665** (2003) 325–366, arXiv:hep-ph/0302135.

[33] S. Catani, D. de Florian, M. Grazzini, and P. Nason, *Soft-gluon resummation for Higgs boson production at hadron colliders*, JHEP **07** (2003) 028, arXiv:hep-ph/0306211.

[34] U. Aglietti, R. Bonciani, G. Degrassi, and A. Vicini, *Two-loop light fermion contribution to Higgs production and decays*, Phys. Lett. **B595** (2004) 432–441, arXiv:hep-ph/0404071.

[35] S. Actis, G. Passarino, C. Sturm, and S. Uccirati, *NLO Electroweak Corrections to Higgs Boson Production at Hadron Colliders*, Phys. Lett. **B670** (2008) 12–17, arXiv:0809.1301 [hep-ph].

[36] D. de Florian and M. Grazzini, *Higgs production at the LHC: updated cross sections at* $\sqrt{s} = 8$ TeV, arXiv:1206.4133 [hep-ph].

[37] C. Anastasiou, S. Buehler, F. Herzog, and A. Lazopoulos, *Inclusive Higgs boson cross-section for the LHC at 8 TeV*, JHEP **1204** (2012) 004, arXiv:1202.3638 [hep-ph].

[38] J. Baglio and A. Djouadi, *Higgs production at the lHC*, JHEP **03** (2011) 055.

[39] M. Ciccolini, A. Denner, and S. Dittmaier, *Strong and electroweak corrections to the production of Higgs+2jets via weak interactions at the LHC*, Phys. Rev. Lett. **99** (2007) 161803, arXiv:0707.0381 [hep-ph].

[40] M. Ciccolini, A. Denner, and S. Dittmaier, *Electroweak and QCD corrections to Higgs production via vector-boson fusion at the LHC*, Phys. Rev. **D 77** (2008) 013002, arXiv:0710.4749 [hep-ph].

[41] K. Arnold et al., *VBFNLO: A parton level Monte Carlo for processes with electroweak bosons*, Comput. Phys. Commun. **180** (2009) 1661–1670, arXiv:0811.4559 [hep-ph].

[42] P. Bolzoni, F. Maltoni, S.-O. Moch, and M. Zaro, *Higgs production via vector-boson fusion at NNLO in QCD*, Phys. Rev. Lett. **105** (2010) 011801, arXiv:1003.4451 [hep-ph].

[43] T. Han and S. Willenbrock, *QCD correction to the p p → W H and Z H total cross- sections*, Phys. Lett. **B 273** (1991) 167–172.

[44] O. Brein, A. Djouadi, and R. Harlander, *NNLO QCD corrections to the Higgs-strahlung processes at hadron colliders*, Phys. Lett. **B 579** (2004) 149–156, arXiv:hep-ph/0307206.

[45] M. L. Ciccolini, S. Dittmaier, and M. Kramer, *Electroweak radiative corrections to associated WH and ZH production at hadron colliders*, Phys. Rev. **D 68** (2003) 073003, arXiv:hep-ph/0306234.

[46] A. Djouadi, J. Kalinowski, and M. Spira, *HDECAY: A program for Higgs boson decays in the standard model and its supersymmetric extension*, Comput. Phys. Commun. **108** (1998) 56–74, arXiv:hep-ph/9704448.

[47] A. Bredenstein, A. Denner, S. Dittmaier, and M. M. Weber, *Precise predictions for the Higgs-boson decay H → WW/ZZ → 4leptons*, Phys. Rev. **D 74** (2006) 013004, arXiv:hep-ph/0604011.

[48] A. Bredenstein, A. Denner, S. Dittmaier, and M. M. Weber, *Radiative corrections to the semileptonic and hadronic Higgs-boson decays H → WW/ZZ → 4 fermions*, JHEP **02** (2007) 080, arXiv:hep-ph/0611234.

[49] M. Botje et al., *The PDF4LHC working group interim recommendations*, 2011. arXiv:1101.0538 [hep-ph].

[50] H.-L. Lai et al., *New parton distributions for collider physics*, Phys. Rev. **D 82** (2010) 074024, arXiv:1007.2241 [hep-ph].

[51] A. D. Martin, W. J. Stirling, R. S. Thorne, and G. Watt, *Parton distributions for the LHC*, Eur. Phys. J. **C 63** (2009) 189–285, arXiv:0901.0002 [hep-ph].

[52] R. D. Ball et al., *Impact of heavy quark masses on parton distributions and LHC phenomenology*, Nucl. Phys. **B 849** (2011) 296–363, arXiv:1101.1300 [hep-ph].

[53] S. Alekhin, S. Alioli, R. D. Ball, V. Bertone, J. Blumlein, et al., *The PDF4LHC working group interim report*, 2011. arXiv:1101.0536 [hep-ph].

[54] T. Melia, P. Nason, R. Rontsch, and G. Zanderighi, W^+W^-, *WZ and ZZ production in the POWHEG BOX*, JHEP **1111** (2011) 078, arXiv:1107.5051 [hep-ph].

[55] T. Binoth, N. Kauer, and P. Mertsch, *Gluon-induced QCD corrections to* $pp \to ZZ \to \ell\bar{\ell}\ell'\bar{\ell}'$, arXiv:0807.0024 [hep-ph].

[56] J. M. Campbell, R. K. Ellis, and C. Williams, *Vector boson pair production at the LHC*, JHEP **07** (2011) 018, arXiv:1105.0020 [hep-ph].

[57] S. Jadach, Z. Was, R. Decker, and J. H. Kuhn, *The tau decay library TAUOLA: Version 2.4*, Comput. Phys. Commun. **76** (1993) 361–380.

[58] P. Golonka et al., *The tauola-photos-F environment for the TAUOLA and PHOTOS packages, release II*, Comput. Phys. Commun. **174** (2006) 818–835.

[59] M. L. Mangano et al., *ALPGEN, a generator for hard multiparton processes in hadronic collisions*, JHEP **07** (2003) 001, arXiv:hep-ph/0206293.

[60] M. L. Mangano, M. Moretti, F. Piccinini, and M. Treccani, *Matching matrix elements and shower evolution for top-quark production in hadronic collisions*, JHEP **01** (2007) 013, arXiv:hep-ph/0611129 [hep-ph].

[61] K. Melnikov and F. Petriello, *Electroweak gauge boson production at hadron colliders through* $O(\alpha_s^2)$, Phys. Rev. **D 74** (2006) 114017, arXiv:hep-ph/0609070.

[62] C. Anastasiou, L. J. Dixon, K. Melnikov, and F. Petriello, *High precision QCD at hadron colliders: Electroweak gauge boson rapidity distributions at NNLO*, Phys. Rev. **D69** (2004) 094008, arXiv:hep-ph/0312266 [hep-ph].

[63] S. Frixione, P. Nason, and B. R. Webber, *Matching NLO QCD and parton showers in heavy flavour production*, JHEP **08** (2003) 007, arXiv:hep-ph/0305252.

[64] M. Aliev et al., *HATHOR: HAdronic Top and Heavy quarks crOss section calculatoR*, Comput. Phys. Commun. **182** (2011) 1034, arXiv:1007.1327 [hep-ph].

[65] G. Corcella et al., *HERWIG 6: an event generator for hadron emission reactions with interfering gluons (including super-symmetric processes)* , JHEP **01** (2001) 010.

[66] J. M. Butterworth, J. R. Forshaw, and M. H. Seymour, *Multiparton interactions in photoproduction at HERA*, Z. Phys. **C 72** (1996) 637–646, arXiv:hep-ph/9601371.

[67] ATLAS Collaboration, *The ATLAS simulation Infrastructure*, Eur. Phys. J. **C 70** (2010) 823–874, arXiv:1005.4568 [physics.ins-det].

[68] S. Agostinelli et al., *GEANT4: A simulation toolkit*, Nucl. Instrum. Meth. **A 506** (2003) 250–303.

[69] ATLAS Collaboration, *Improved electron reconstruction in ATLAS using the Gaussian Sum Filter-based model for bremsstrahlung*, ATLAS-CONF-2012-047 (2012) .

[70] ATLAS Collaboration, *Electron performance measurements with the ATLAS detector using the 2010 LHC proton-proton collision data*, Eur. Phys. J. **C72** (2012) 1909, arXiv:1110.3174 [hep-ex].

[71] ATLAS Collaboration, *Measurement of the $W \to \ell\nu$ and $Z/\gamma^* \to \ell\ell$ production cross sections in proton-proton collisions at $\sqrt{s} = 7$ TeV with the ATLAS detector*, JHEP **12** (2010) 060, arXiv:1010.2130 [hep-ex].

[72] ATLAS Collaboration, *Measurements of the electron and muon inclusive cross-sections in proton-proton collisions at $\sqrt{s} = 7$ TeV with the ATLAS detector*, Phys. Lett. **B707** (2012) 438–458, arXiv:1109.0525 [hep-ex].

[73] R. Frühwirth, *Track fitting with non-Gaussian noise*, Comput. Phys. Commun. **100** (1997) no. 1-2, 1 – 16.

[74] A. L. Read, *Presentation of search results: The CL(s) technique*, J. Phys. G **28** (2002) 2693–2704.

[75] G. Cowan, K. Cranmer, E. Gross, and O. Vitells, *Asymptotic formulae for likelihood-based tests of new physics*, Eur. Phys. J. **C 71** (2011) 1554, arXiv:1007.1727 [physics.data-an].

[76] E. Gross and O. Vitells, *Trial factors for the look elsewhere effect in high energy physics*, Eur. Phys. J. **C 70** (2010) 525–530, arXiv:1005.1891 [physics.data-an].

[77] ATLAS and C. Collaborations, *Combined Standard Model Higgs boson searches with up to 2.3 fb^{-1} of pp collisions at $\sqrt{s} = 7$ TeV at the LHC*, ATLAS-CONF-2011-157 (2011) .

A Auxiliary material

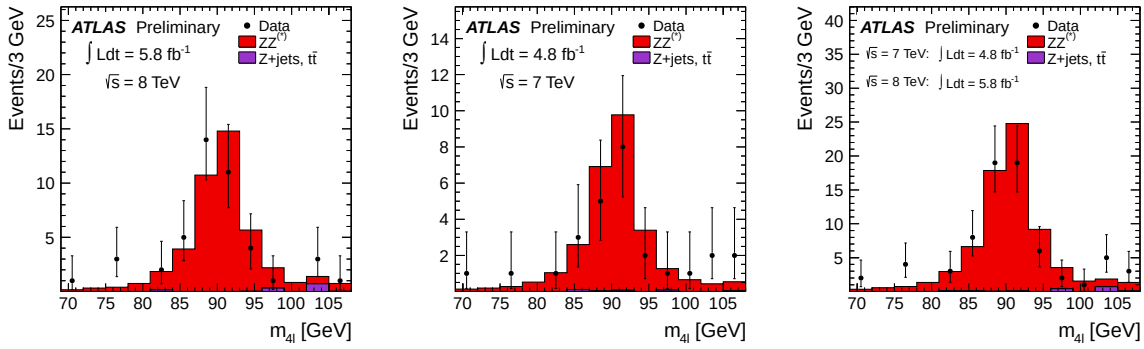

(a) (b) (c)

Figure 18: Invariant mass of the four leptons, combining all final states, demonstrating the single-resonant peak $pp \to Z \to 4\ell$. To improve the acceptance the following modifications were performed to the nominal analysis: the requirement on m_{12} is relaxed to 30 GeV $< m_{12} <$ 106 GeV, the requirement on m_{34} is relaxed to 5 GeV $< m_{34} <$ 115 GeV, and the p_{T} requirement on the softest muon was relaxed to $p_{\mathrm{T}} > 4$ GeV. For 4μ events, the requirement on the third muon is $p_{\mathrm{T}} > 8$ GeV. The data are shown for (a) $\sqrt{s} = 8$ TeV, (b) $\sqrt{s} = 7$ TeV and (c) combined.

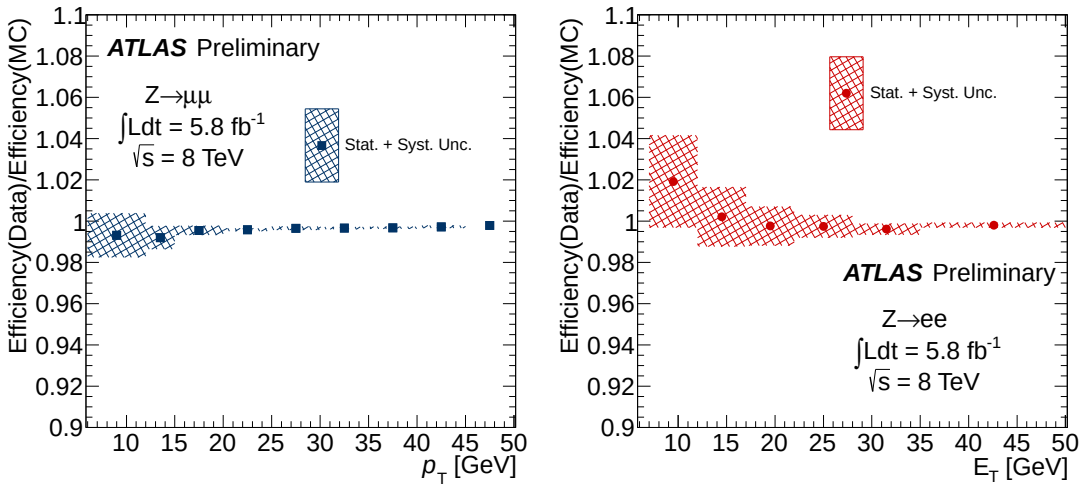

(a) (b)

Figure 19: Ratio of the isolation and impact parameter efficiencies between data and simulation, estimated with the Tag & Probe method, using (a) $Z \to \mu\mu$ and (b) $Z \to ee$ events.

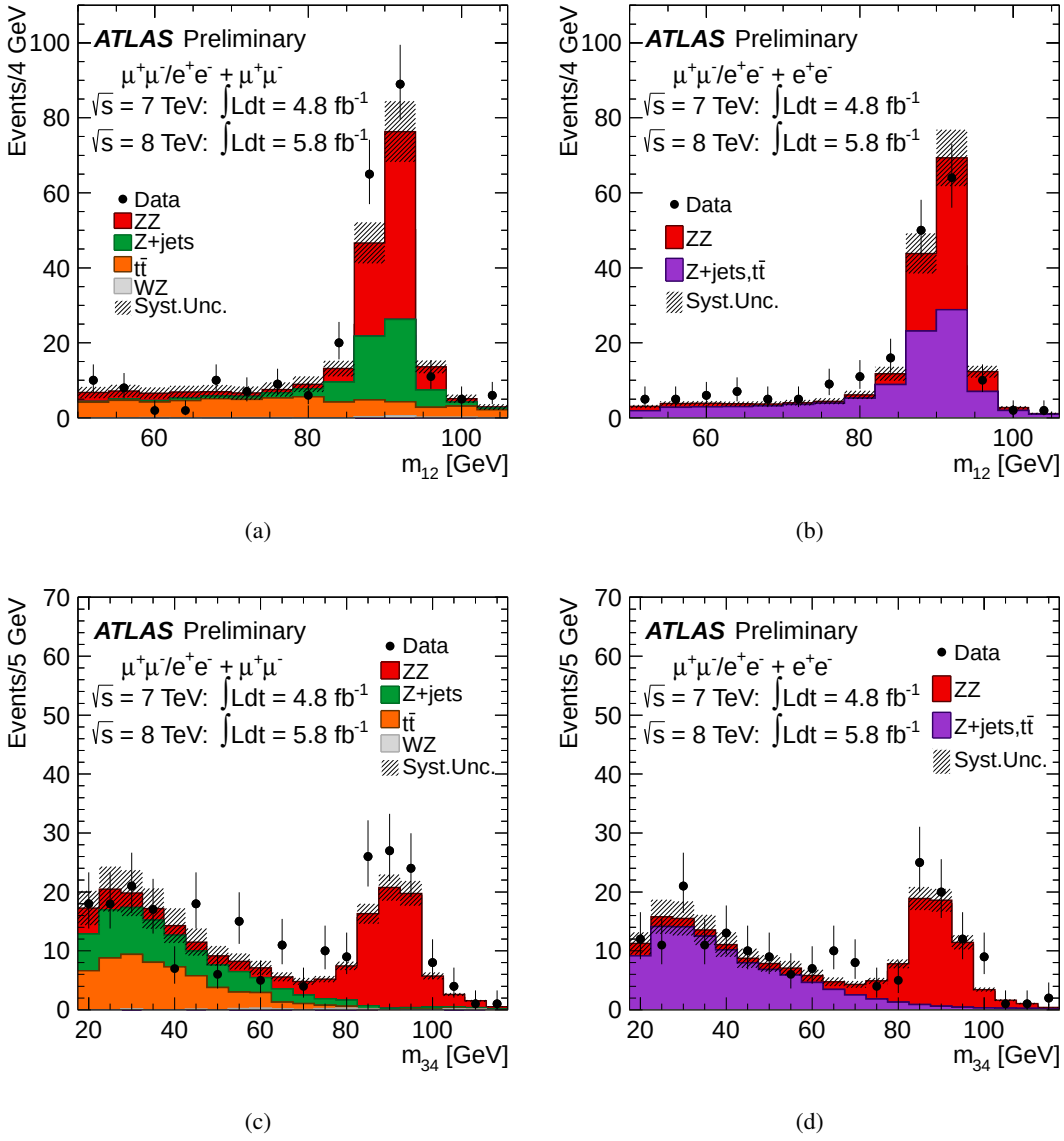

Figure 20: Invariant mass distributions of the lepton pairs in the control sample defined by a Z boson candidate and an additional same-flavour lepton pair, for the $\sqrt{s}$ = 8 TeV and $\sqrt{s}$ = 7 TeV datasets combined. The sample is divided according to the flavour of the additional lepton pair. In (a) the m_{12} and in (c) the m_{34} distributions are presented for $\ell\ell + \mu\mu$ events. In (b) the m_{12} and in (d) the m_{34} distributions are presented for $\ell\ell + ee$ events. The kinematic selection of the analysis is applied. Isolation and impact parameter significance requirements are applied to the first lepton pair only. The MC is normalized to the data driven background estimations.

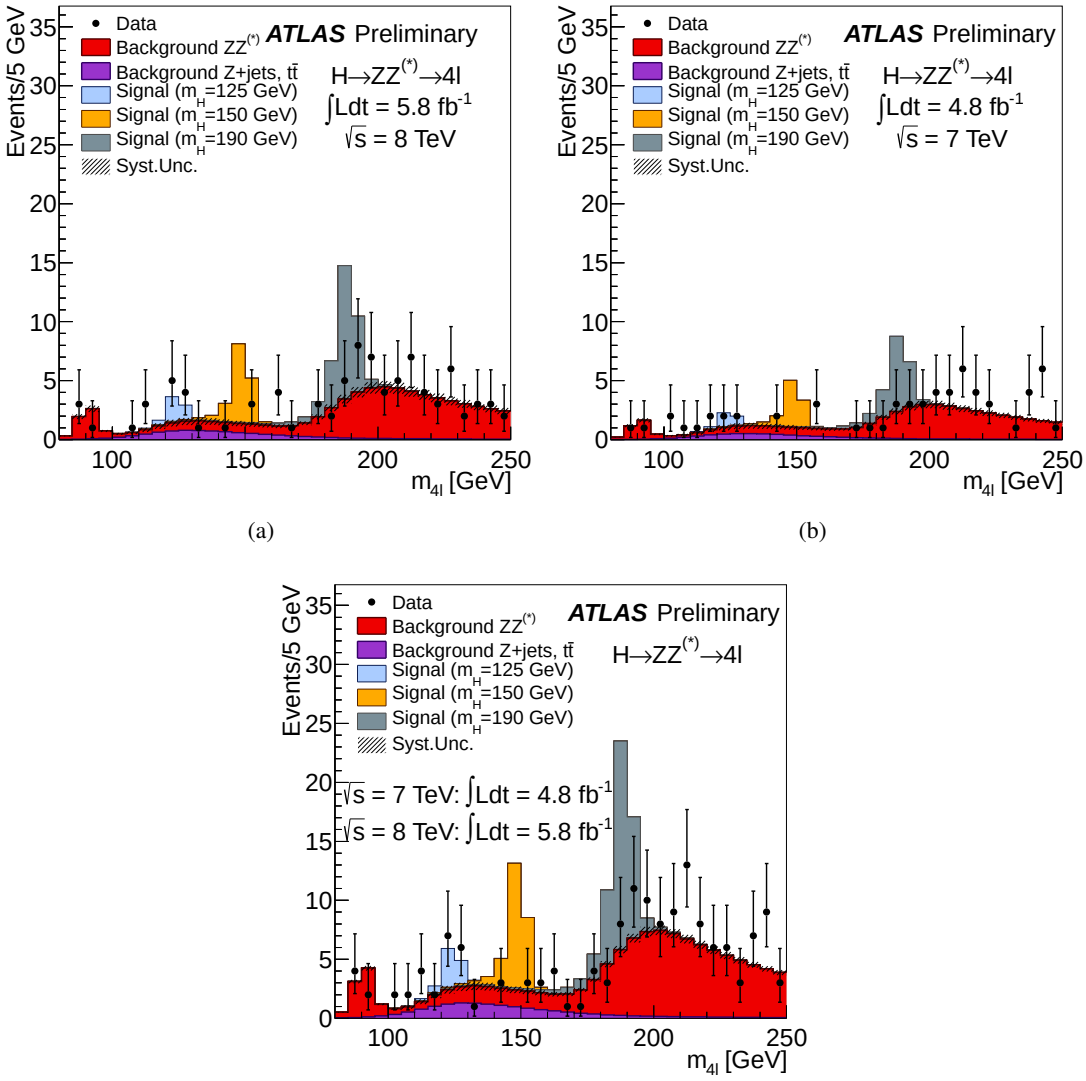

(a)

(b)

(c)

Figure 21: The distribution of the four-lepton invariant mass, $m_{4\ell}$, for the selected candidates compared to the background expectation for the $80-250$ GeV mass range for the (a) $\sqrt{s} = 8$ TeV, (b) $\sqrt{s} = 7$ TeV and (c) combined datasets. Error bars represent 68.3% central confidence intervals. The signal expectation for several m_H hypotheses is also shown.

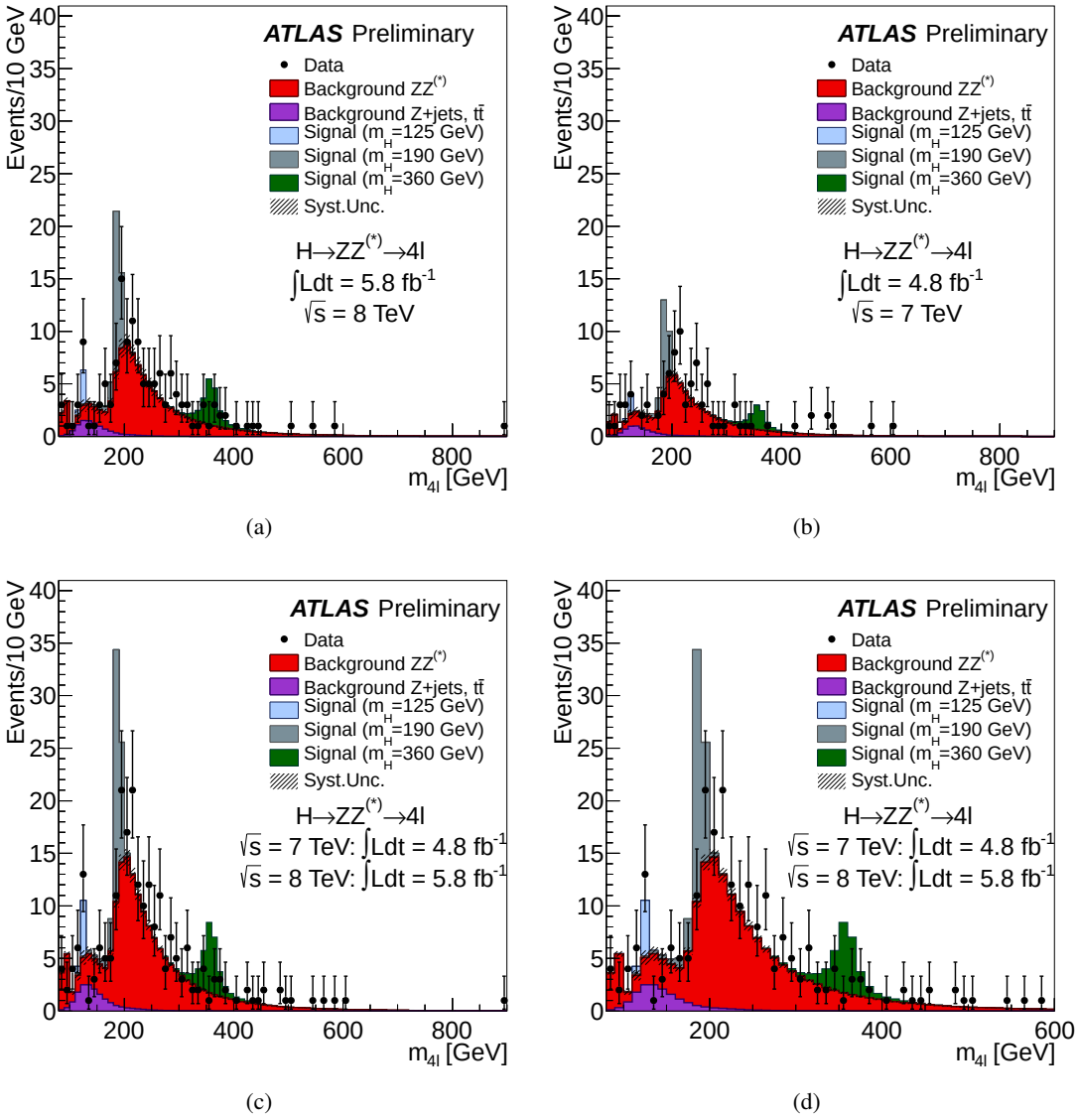

Figure 22: The distribution of the four-lepton invariant mass, $m_{4\ell}$, for the selected candidates for the combination of both analyses, compared to the background expectation. The $\sqrt{s} = 8$ and $\sqrt{s} = 7$ TeV datasets are shown separately in (a) and (b), respectively, and combined in (c). The combined result in the range $80-600$ GeV is also shown (d). Error bars represent 68.3% central confidence intervals. The signal expectation for several m_H hypotheses is also shown.

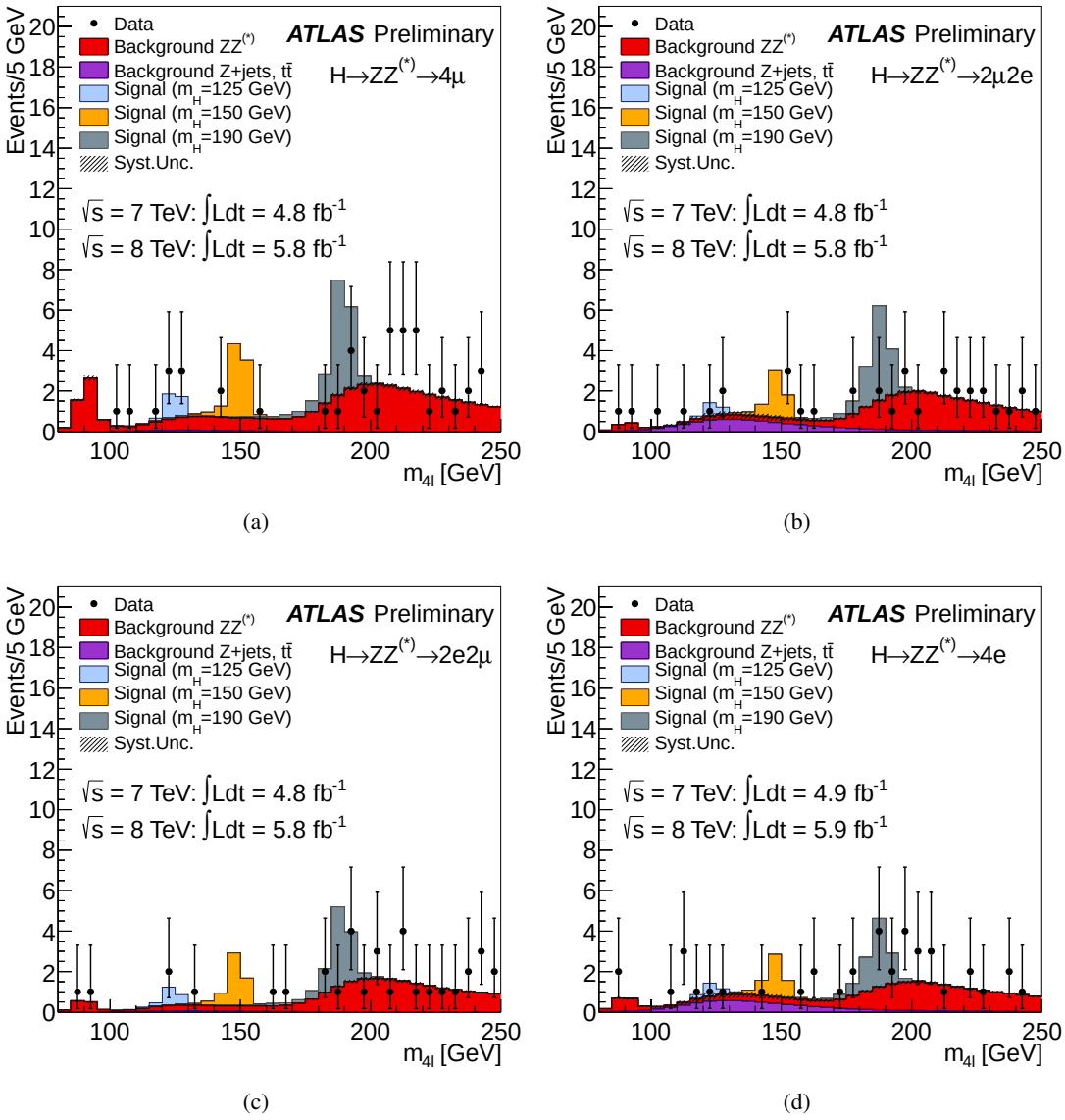

Figure 23: The distribution of the four-lepton invariant mass, $m_{4\ell}$, for the selected candidates for the combination of both analyses for the various sub-channels, (a) 4μ , (b) $2\mu 2e$, (c) $2e2\mu$, (d) $4e$, compared to the background expectation for the $80-250$ GeV mass range. Error bars represent 68.3% central confidence intervals. The signal expectation for several m_H hypotheses is also shown.

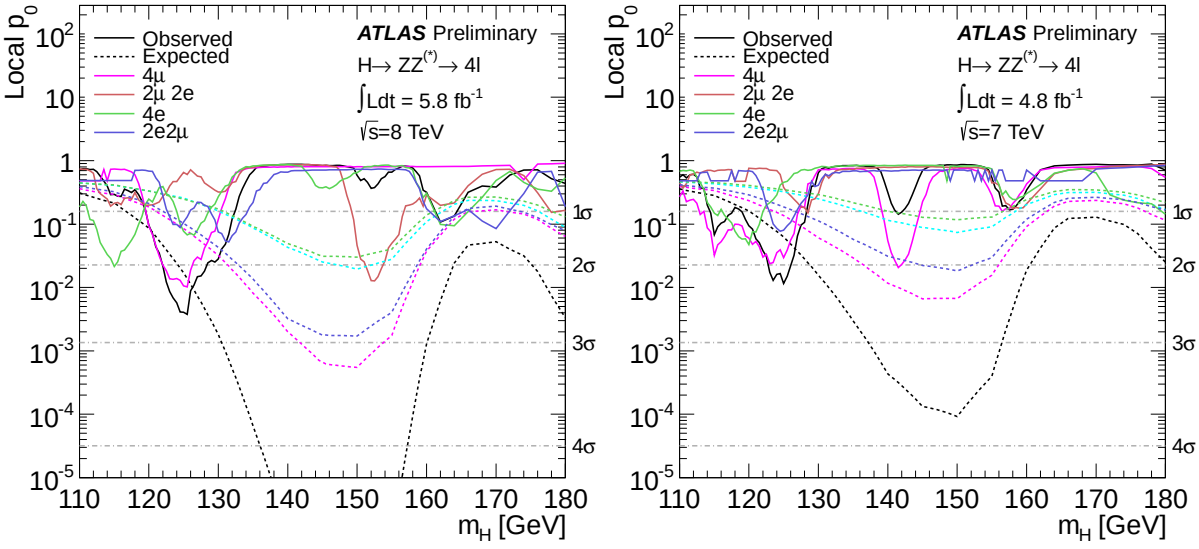

(a) (b)

Figure 24: Observed local p_0, the probability that the background fluctuates to the observed number of events or higher, for each analysis sub-channel, and for their combination. Dashed curves show the expected median local p_0 for the signal hypothesis when tested at m_H; (a) 2012 ($\sqrt{s} = 8$ TeV) data, (b) 2011 ($\sqrt{s} = 7$ TeV) data.

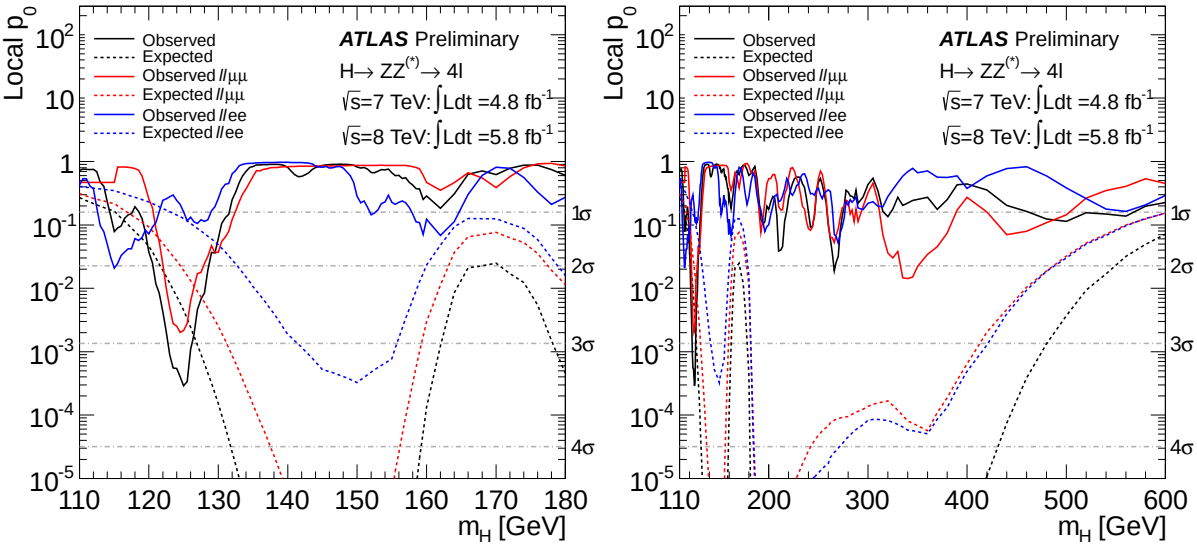

(a) (b)

Figure 25: Observed local p_0, the probability that the background fluctuates to the observed number of events or higher, separating the two analyses with sub-leading muons ($\ell\ell\mu\mu$) from the two analyses with sub-leading electrons ($\ell\ell ee$); the black line shows the combined result. Dashed curves show the expected median local p_0 for the signal hypothesis when tested at m_H; (a) low mass region, (b) full mass range.

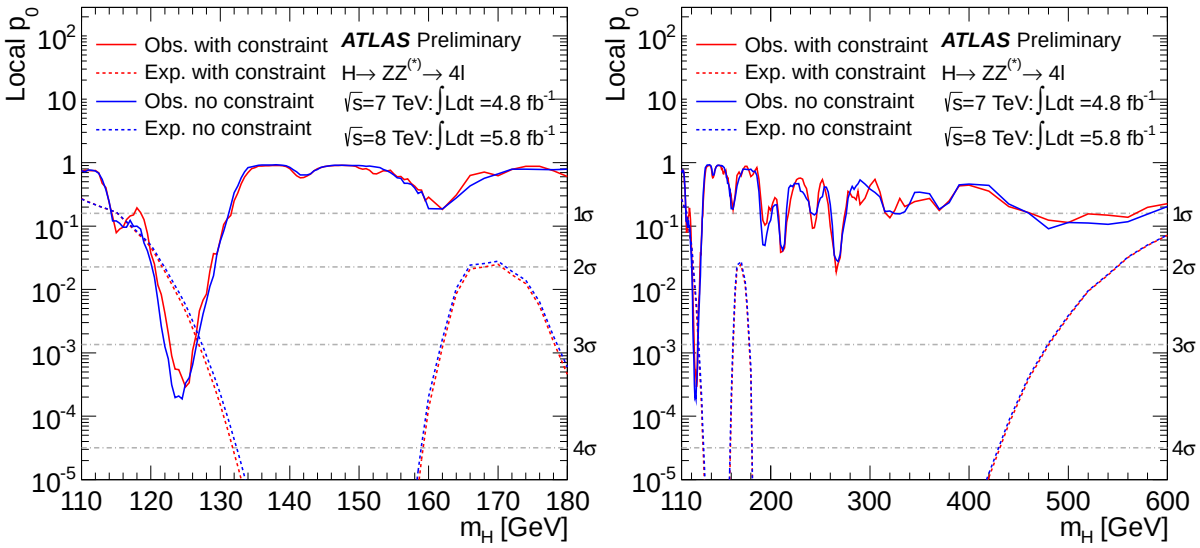

(a) (b)

Figure 26: Observed local p_0, the probability that the background fluctuates to the observed number of events or higher, before and after the application of a Z mass constraint. Dashed curves show the expected median local p_0 for the signal hypothesis when tested at m_H; (a) low mass region, (b) full mass range.

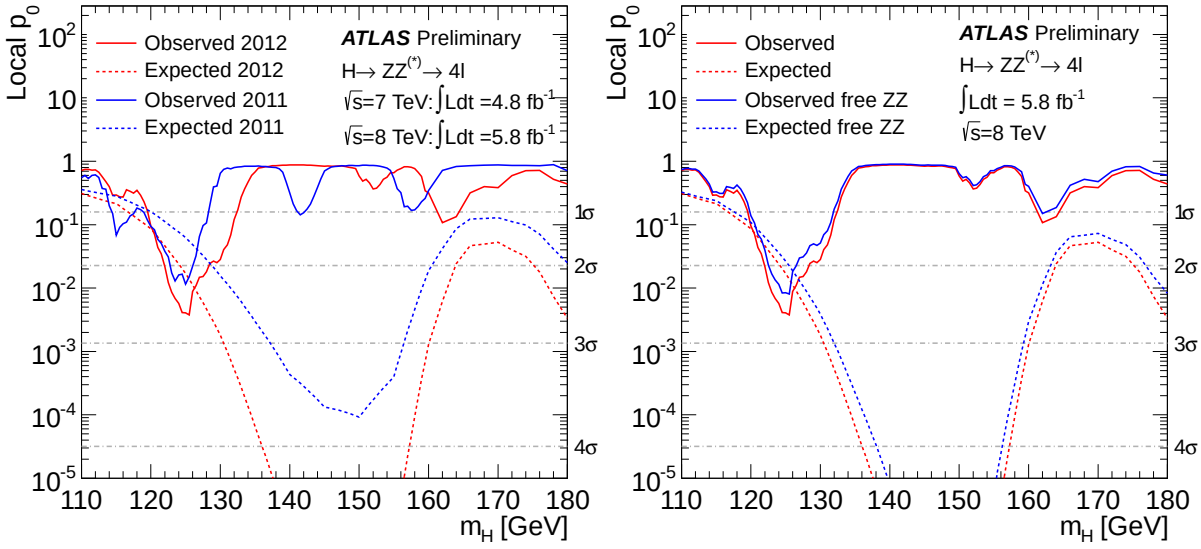

(a) (b)

Figure 27: The observed local p_0, the probability that the background fluctuates to the observed number of events or higher, is shown as solid lines. The dashed curve shows the expected median local p_0 for the signal hypothesis when tested at m_H. (a) compares the local p_0 for the $\sqrt{s} = 8$ TeV and the $\sqrt{s} = 7$ TeV data samples; (b) shows the effect of allowing the irreducible background normalisation to float freely in the fit, for the $\sqrt{s} = 8$ TeV data sample. The horizontal dashed lines indicate the p_0 values corresponding to local significances of 1σ, 2σ, 3σ and 4σ.

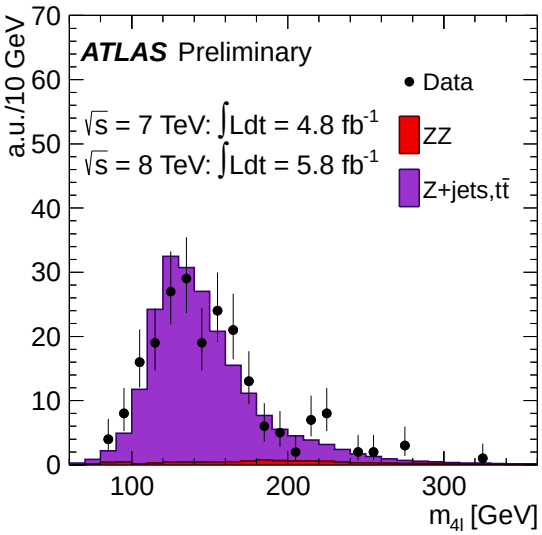

Figure 28: Shape comparison of the $m_{4\ell}$ distribution used for the Z+jets and $t\bar{t}$ contributions, in a control region where the sub-leading di-lepton fails either the isolation or the impact parameter significance requirements of the analysis, for both the $\sqrt{s} = 7$ TeV and $\sqrt{s} = 8$ TeV data samples.

B Event Displays

B.1 EventNumber: 82614360 RunNumber: 203602

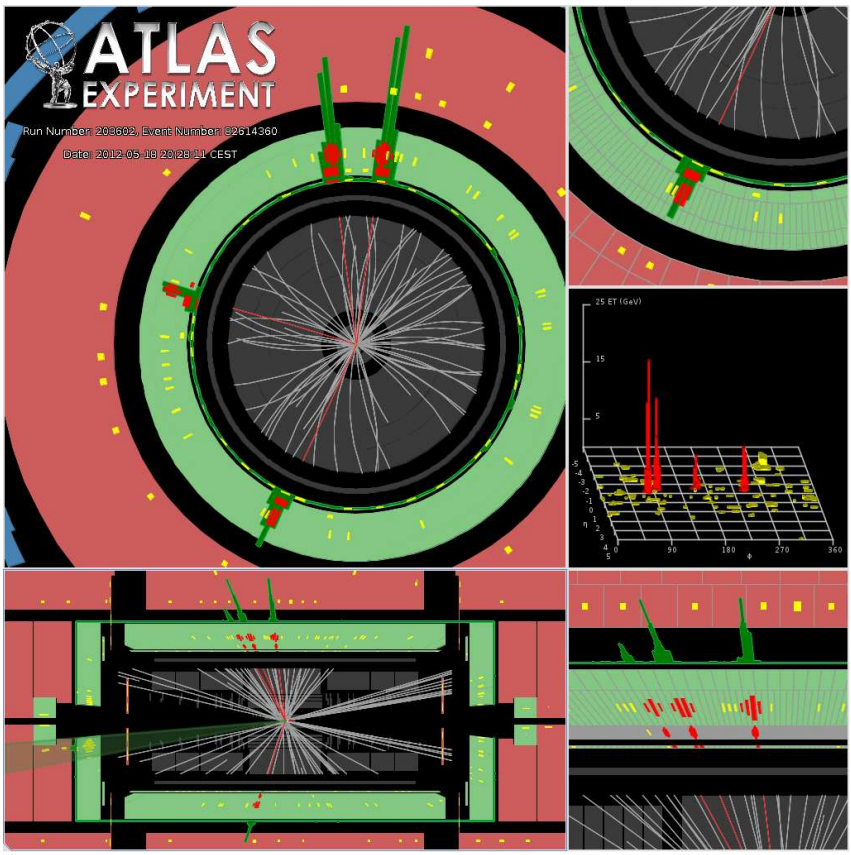

Figure 29: Event display of a 4e candidate. EventNumber: 82614360 RunNumber: 203602 $m_{4\ell}$ = 124.6 GeV. m_{12} = 70.6 GeV, m_{34} = 44.7 GeV. e_1 : p_{T} = 24.9 GeV, η = −0.33, ϕ = 1.98. e_2 : p_{T} = 53.9 GeV, η = −0.40, ϕ = 1.69. e_3 : p_{T} = 61.9 GeV, η = −0.12, ϕ = 1.45. e_4 : p_{T} = 17.8 GeV, η = −0.51, ϕ = 2.84.

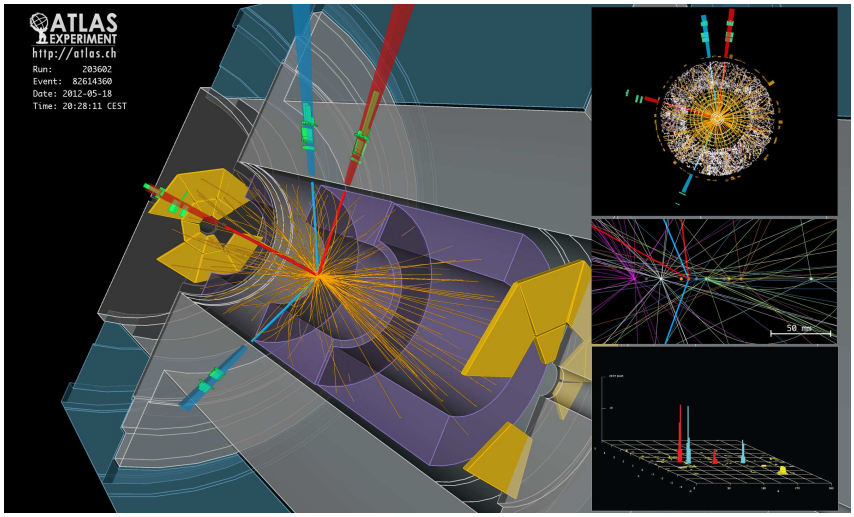

Figure 30: Event display of a 4e candidate. EventNumber: 82614360 RunNumber: 203602 $m_{4\ell}$ = 124.6 GeV. m_{12} = 70.6 GeV, m_{34} = 44.7 GeV. e_1 : p_{T} = 24.9 GeV, η = −0.33, ϕ = 1.98. e_2 : p_{T} = 53.9 GeV, η = −0.40, ϕ = 1.69. e_3 : p_{T} = 61.9 GeV, η = −0.12, ϕ = 1.45. e_4 : p_{T} = 17.8 GeV, η = −0.51, ϕ = 2.84.

B.2 EventNumber: 82599793 RunNumber: 204769

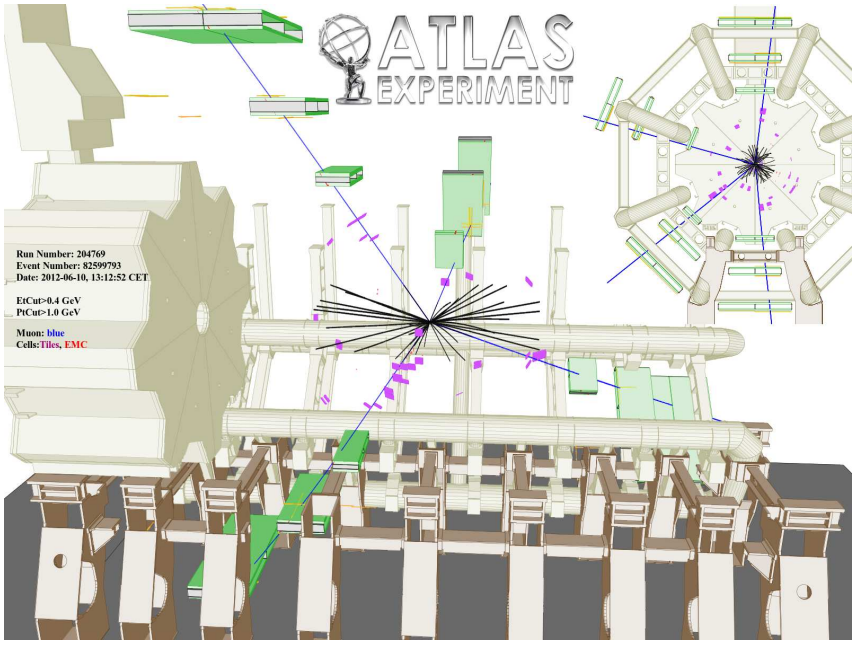

Figure 31: Event display of a 4μ candidate. EventNumber: 82599793 RunNumber: 204769 $m_{4\ell}$ = 123.5 GeV. m_{12} = 84 GeV, m_{34} = 34.2 GeV.μ_1 : p_{T} = 37.8 GeV, η = 0.61 ϕ = 1.46. μ_2 : p_{T} = 29.2 GeV, η = −0.95, ϕ = −2.47. μ_3 : p_{T} = 10.3 GeV, η = 0.62 ϕ = −1.41. μ_4 : p_{T} = 32.6 GeV η = −0.16, ϕ = 2.85.

B.3 EventNumber: 71402630 RunNumber: 204769

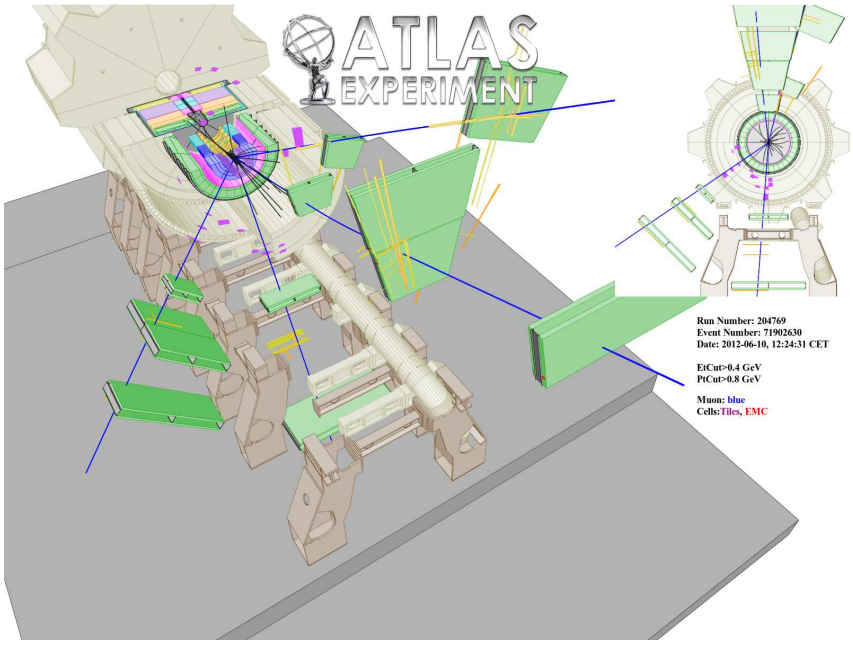

Figure 32: Event display of a 4μ candidate. EventNumber: 71902630 RunNumber: 204769 $m_{4\ell}$ = 125.1 GeV. m_{12} = 86.3 GeV, m_{34} = 31.6 GeV. μ_1 : p_{T} = 36.1 GeV, η = 1.29, ϕ = 1.33. μ_2 : p_{T} = 47.5 GeV, η = 0.69, ϕ = −1.65. μ_3 : p_{T} = 26.4 GeV, η = 0.47, ϕ = −2.51. μ_4 : p_{T} = 71.7 GeV, η = 1.85, ϕ = 1.65.

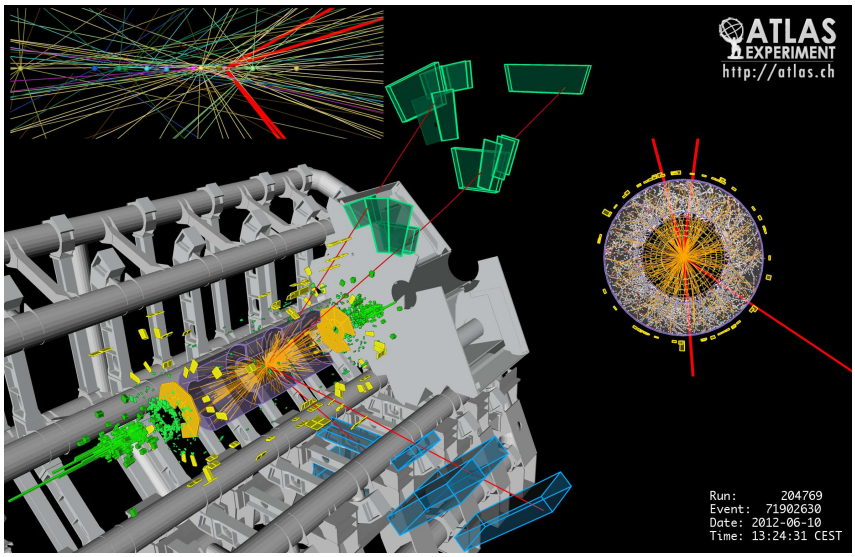

Figure 33: Event display of a 4μ candidate. EventNumber: 71902630 RunNumber: 204769 $m_{4\ell}$ = 125.1 GeV. m_{12} = 86.3 GeV, m_{34} = 31.6 GeV. μ_1 : p_{T} = 36.1 GeV, η = 1.29, ϕ = 1.33. μ_2 : p_{T} = 47.5 GeV, η = 0.69, ϕ = −1.65. μ_3 : p_{T} = 26.4 GeV, η = 0.47, ϕ = −2.51. μ_4 : p_{T} = 71.7 GeV, η = 1.85, ϕ = 1.65.

B.4 EventNumber: 12611816 RunNumber: 205113

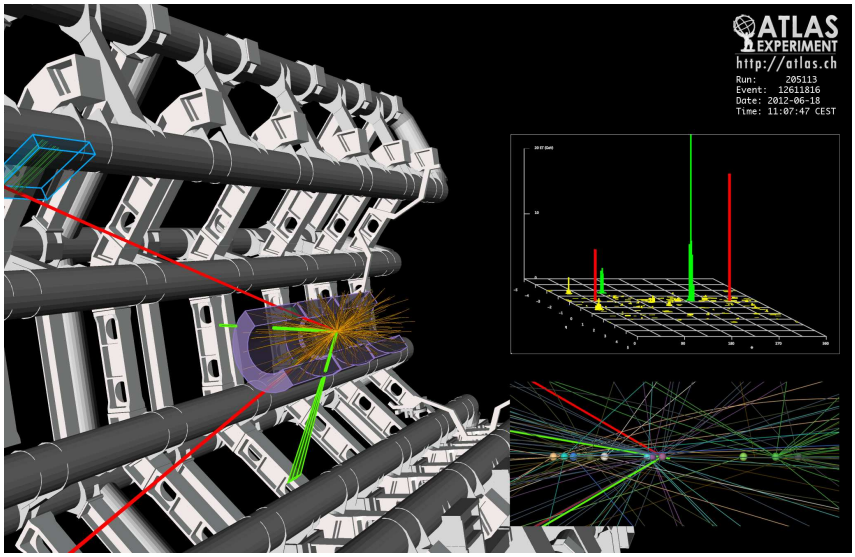

Figure 34: Event display of a $2e2\mu$ candidate. EventNumber: 12611816 RunNumber: 205113 $m_{4\ell}$ = 123.9 GeV. m_{12} = 87.9 GeV, m_{34} = 19.6 GeV. e_1 : p_{T} = 18.7 GeV, η = −2.45, ϕ = 1.68. e_2 : p_{T} = 75.96 GeV, η = −1.16, ϕ = −2.13. μ_3 : p_{T} = 19.6 GeV, η = −1.14, ϕ = −0.87. μ_4 : p_{T} = 7.9 GeV, η = −1.13, ϕ = 0.94.